CHARACTERIZATION OF CYLINDRICAL NANO-DOMAINS IN THIN FILMS OF POLYSTYRENE-POLY(METHYL METHACRYLATE) DIBLOCK COPOLYMER STUDIED VIA ATOMIC FORCE MICROSCOPY

by

HELENE C. MAIRE

B. S. University of Nice Sophia-Antipolis (France), 2002

AN ABSTRACT OF A DISSERTATION
submitted in partial fulfillment of the requirements for the degree

DOCTOR OF PHILOSOPHY

Department of Chemistry
College of Arts and Sciences

KANSAS STATE UNIVERSITY
Manhattan, Kansas

2008

Abstract

We have investigated the orientation of cylindrical domains in thin films of a polystyrene–poly(methylmethacrylate) diblock copolymer (PS-*b*-PMMA) on planar substrates having different surface roughnesses and hydrophilicities. The research in this dissertation covers the substrate surface modifications, the enhancement of the diblock copolymer film coating, and the refinement of the treatments leading to nanoporous material.

Treatment of the substrate with organic mercaptans forming self-assembled-monolayer (SAM), leading to various hydrophilicities of the surfaces, was inconclusive as far as orienting the PMMA domains in the PS matrix due to thermal instability of some thiols. This directed us to a different approach involving substrate roughness. PS-*b*-PMMA films of 20~200 nm thick were prepared via spin-coating on silicon, gold or indium tin oxide (ITO) substrates, and annealed in vacuum at 170 °C for 60 hours to induce the formation of cylindrical PMMA domains. Atomic force microscopy (AFM) images indicated the domain orientation at the free surface. In PS-*b*-PMMA films much thicker than the domain periodicity (L_0), the domains were oriented perpendicularly to the free surface regardless of underlying substrates, reflecting the balanced interactions of PS and PMMA blocks at the polymer–vacuum interface. In films having thickness similar to L_0, vertically oriented domains were observed on the Au and ITO surfaces that are covered with nanoscale grains, whereas horizontal domains were observed on the smooth Si substrates. In particular, the cylindrical PMMA domains were efficiently perpendicularly aligned when the grain size nearly was equal to L_0. The perpendicular domain alignment induced by the substrate roughness was corroborated using cyclic voltammetry (CV) for gold substrates coated with PS-*b*-PMMA films whose PMMA domains were removed by UV and subsequent acetic acid treatments. The CV data also suggested that

the PMMA domains were successfully removed, leaving a nanoporous stable PS matrix on the substrate.

CHARACTERIZATION OF CYLINDRICAL NANO-DOMAINS IN THIN FILMS OF POLYSTYRENE-POLY(METHYLMETHACRYLATE) DIBLOCK COPOLYMER STUDIED VIA ATOMIC FORCE MICROSCOPY

By

HELENE C. MAIRE
B. S. University of Nice Sophia-Antipolis (France), 2002

A DISSERTATION
submitted in partial fulfillment of the requirements for the degree

DOCTOR OF PHILOSOPHY

Department of Chemistry
College of Arts and Sciences

KANSAS STATE UNIVERSITY
Manhattan, Kansas
2008

Approved by:

Major Professor:
Dr Takashi Ito

Abstract

We have investigated the orientation of cylindrical domains in thin films of a polystyrene–poly(methylmethacrylate) diblock copolymer (PS-*b*-PMMA) on planar substrates having different surface roughnesses and hydrophilicities. The research in this dissertation covers the substrate surface modifications, the enhancement of the diblock copolymer film coating, and the refinement of the treatments leading to nanoporous material.

Treatment of the substrate with organic mercaptans forming self-assembled-monolayer (SAM), leading to various hydrophilicities of the surfaces, was inconclusive as far as orienting the PMMA domains in the PS matrix due to thermal instability of some thiols. This directed us to a different approach involving substrate roughness. PS-*b*-PMMA films of 20~200 nm thick were prepared via spin-coating on silicon, gold or indium tin oxide (ITO) substrates, and annealed in vacuum at 170 °C for 60 hours to induce the formation of cylindrical PMMA domains. Atomic force microscopy (AFM) images indicated the domain orientation at the free surface. In PS-*b*-PMMA films much thicker than the domain periodicity (L_0), the domains were oriented perpendicularly to the free surface regardless of underlying substrates, reflecting the balanced interactions of PS and PMMA blocks at the polymer–vacuum interface. In films having thickness similar to L_0, vertically oriented domains were observed on the Au and ITO surfaces that are covered with nanoscale grains, whereas horizontal domains were observed on the smooth Si substrates. In particular, the cylindrical PMMA domains were efficiently perpendicularly aligned when the grain size nearly was equal to L_0. The perpendicular domain alignment induced by the substrate roughness was corroborated using cyclic voltammetry (CV) for gold substrates coated with PS-*b*-PMMA films whose PMMA domains were removed by UV and subsequent acetic acid treatments. The CV data also suggested that

the PMMA domains were successfully removed, leaving a nanoporous stable PS matrix on the substrate.

Table of Contents

List of Figures

List of Tables

Acknowledgements

I would like to thank my research advisor, Dr Ito, for his availability and constant presence over the years spent working in his laboratory. I remember how we started with empty rooms, to finally end up with a nicely organized and practical laboratory.

I have had the pleasure to work with few post-docs, graduate students, and undergraduate students over the years in Dr Ito’s group, namely: Dr Yongxin Li, Dr Ahmad A. Audi, Shaida Ibrahim, Neluni Perrera, Bipin Pandey, Li Feng, Gregory Dible, and Sarah Foreman. We have shared not only chemistry but also culture. In their own different ways, they all taught me something, and I am grateful for that. I thank Prof. Christopher Culbertson (Department of Chemistry, Kansas State University) for providing access to the profilometer and the microscope used for part of this study, as well as Gregory Roman and Amanda Meyer for their help using these instruments. I thank Prof. Daniel Higgins (Department of Chemistry, Kansas State University) for providing the ITO substrates, Dr Yongxin Li for his work on the electrochemical measurements, Li Feng for the synthesis of thiols, and Shaida Ibrahim and Shinobu Ito for their assistance with PS-*b*-PMMA film preparation. I would also want to express my gratitude to my colleagues from the Chemistry Department at Kansas State University for their time and support, especially Prof. Eric Maatta.

In addition, I would like to thank my friends, my family, and all the people that helped me during these years; thank you for your support, your nice words, your prayers, your time, your ability and availability to listen, your smiles, and all the laughs we have shared even during difficult times. The list would be endless, so my friends and family will recognize themselves. However, I will specifically cite Dr Joyce A. Woodford, and Heather M. Reed.

Continual financial support of this work was greatly appreciated.

Dedication

To all women who cannot freely study.

CHAPTER 1 - Introduction

There is considerable interest these days in the fabrication of nanometer-scale devices and features. Devices or features of this size can be used in many different ways, such as for catalytic supports, chemical sensors, photonic materials, solid-state electrochemical devices, and biosensors. To be a nanometer-scale device, the system needs to have at least one dimension in the range 1 to 100nm, such as the nanoporous device considered here. A new way of creating a nanometer-scale porous membrane on an electrode exhibiting unique transport behavior compared to a simple planar electrode was investigated. There are two ways to consider the fabrication of such a device: "top-down" (creating nanostructures in a system), and "bottom-up" (building a nanosystem). The later was the route followed to create a new nanoporous sensor. The challenge is to orient cylindrical domains perpendicularly to the substrate surface in order to form these nanopores. This dissertation presents a way to induce the orientation of cylindrical nanodomains in thin films of polystyrene-poly(methylmethacrylate) diblock copolymer and to characterize them via AFM.

Motivations and Objectives

This project was designed to develop, in the long term, a new nanoporous sensor by combining a diblock copolymer [1-13] and a treated conducting substrate, and to finally characterize the orientation of the nanodomains formed using atomic force microscopy (AFM) as well as cyclic voltammetry (CV) measurements. This device would execute different tasks, such as pre-concentration, selective ion transport, and separation of compounds based on unique, because based on its nanometer-scale pores, mass transport behavior. This system would be classified as a nanoporous polymer film on electrode. The nanometer-scale size of the pores obtained through this design is essential to achieve efficient separation, and detection.

According to Bates and Fedrickson, a diblock copolymer is a "macromolecule composed of sequences, or blocks, of chemically distinct repeat unit" [9]. This design incorporates a diblock copolymer, here polystyrene-poly(methyl methacrylate) (PS-*b*-

PMMA), as the generator of nanoporous film [4, 10], a gold-coated silicon wafer as the conducting substrate, and organic mercaptans as the property modifier at the gold/polymer interface [14-25], in the first part of the dissertation.

In a second part, a design incorporating diblock copolymer PS-*b*-PMMA, as the generator of nanoporous film [4, 10], and various substrates such as gold-coated silicon wafers (Au-Si), indium-tin-oxide (ITO) coated cover slips, gold-coated glass slides (Au-glass), and silicon wafers (Si) is described. This part is a study of the relationship between the diblock copolymer domains orientation and the substrate's roughness.

Both designs involved AFM imaging to characterize the diblock copolymer films. Only the latest design uses CV measurements to assess the completeness of the nanopore formation in the diblock copolymer films. Each analytical technique used for this research is presented in Chapter 2.

Nanoporous Membranes

Nanometer-scale pores have unique characteristics for mass transport behavior, and have various applications for chemical sensing. There are different types of membranes containing nanometer-scale pores: molecular membranes [27], anodized alumina membranes [28], and track etched membranes [29]. Although anodized alumina and track-etched membranes can be commercially available, it is possible to control the size of the pores by coating the pore surface via electroless metal [29] or sol-gel deposition [28]. For molecular membrane, its pore size is determined by the intramolecular cavity [27]. Additionally, the efficiency and selectivity of analyte transport can be controlled by chemically modifying the surfaces of the nanometer-scale pores on the basis of chemical interactions between the transported analytes and the inside walls of the pores [28, 29]. For example, the surface of nanometer-scale pores within gold-coated track etched membranes can be modified with self assembled monolayers (SAMs) of organic mercaptans as attempted in the first part of this project [29], and SiO_2 gel-coated pores can be functionalized via silane chemistry [28]. Chemical sensing based on mass transport of analytes through nanometer-scale porous membranes includes for instance separation of molecules of different sizes, the separation of enantiomers [28], the separation of proteins having similar sizes but different shapes [29], the separation of single-stranded DNA molecules with single base mismatches [30], and the detection of molecule based on the change in Ca^{2+} flow within the pores [31]. Track-etched membranes and nanoporous alumina membranes have also been used as templates for silica or metal nanowire growth [6, 32, 33] as well as masks for lithography [5, 34], for virus filtration [35], and for nanoparticles electrophoretic deposition [36].

Block copolymers (BCPs) [37-40] containing self-organized nanoscale domains have recently been employed to fabricate masks for lithography,[41] templates for metal or silica nanowire synthesis,[6,32] templates for nanoparticles deposition,[36, 42] and filtration membranes for viruses.[35] In particular, BCPs that form cylindrical domains of the minor component[37-40] have been used to fabricate monoliths containing an array of uniform nanopores by chemically etching the minor component.[10, 57, 58] BCPs are special in a way that they can rearrange and form various types of domains of one block into another depending on their volume ratio, as shown in Figure 1-1.[9] For the aforementioned applications, it is important to control both the diameter and the alignment of the cylindrical domains in BCP monoliths. Whereas the domain diameter can be controlled by changing the molecular weight of the BCP, [37-40] it is often challenging to control the alignment of the domains.

There are numerous ways to induce a domain orientation into a diblock copolymer film such as in plane electric fields [47], temperature gradients, directional solidification, and chemically nanopatterned substrate either with random copolymer brush [47], or SAM [4, 24]. Some groups have been using thick BCP films; others have employed difficult and time-consuming procedures. This research investigated a simpler way to orient domains into BCP thin films. First, by exploring the relationship between the domains orientation in the diblock copolymer films and the surface energy of the substrate given by the type of SAM coating it. Second, by studying the effects of the roughness substrates on the orientation of the domains in BCP thin films.

Self Assembled Monolayers (SAM)

SAMs were used to change the surface properties of the substrate. The generic structure of organic mercaptans used to synthesize films consists of a thiol function at one end, an alkyl chain, and a functional head group at the other extremity.

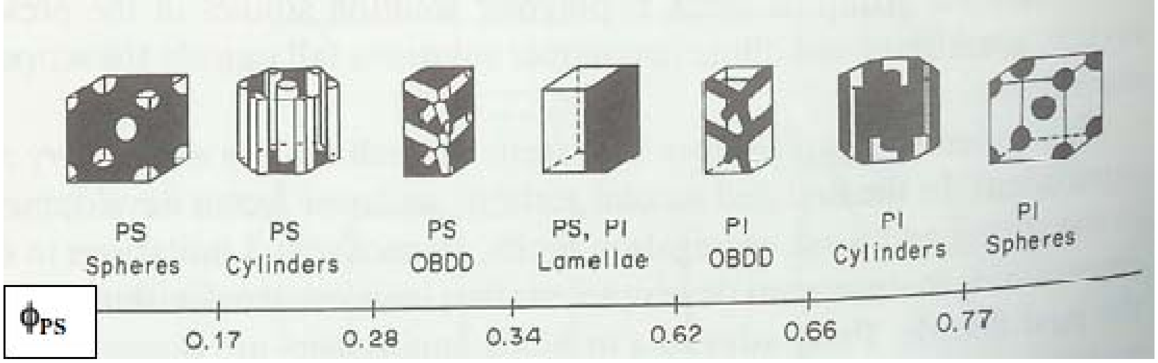

Figure 1-1Rearrangement of $(PS\text{-}PI)_n$ Depending on Φ_{PS}. PS in white, PI in black. [9]

The functional group can be changed as needed [19-20]; therefore it is possible to tailor the properties of a SAM, such as wettability [18-20, 59-62].

A chemical functional group sits at its end. A SAM has such a high affinity for the substrate that it can displace adsorbed organic material from the surface [16]. Oxidative adsorption occurs, creating a metal-sulfur bond as shown in Equation 1.

Equation 1. $Au + RS^- \leftrightarrow Au\text{-}SR + e\text{-}$

The chemisorbed structure adopts structural arrangements as a simple sulfur ad-layer on gold [63]. Therefore, it forms a flexible, well-defined film having the capacity to be simply tailored in order to vary the interfacial properties of the substrate[18-20, 59-62]. The molecular components of SAMs are responsible for its flexibility, and its thickness. There exist various types of thiols that can be used to form SAM on the substrate having different sizes and shapes. Choosing the appropriate thiols is crucial to achieve the suitable conditions, such as wettability of the substrate, to go on with the experiment.

The goal here was to incorporate a specific molecular species in SAM in order to obtain the same new property continuously all over the surface of the substrate [24, 60]. In other words, different n-alkane thiols were mixed to obtain a suitable wettability of the gold-coated wafer.

There are three ways to mix organic mercaptans [25]: adsorption of asymmetric disulfides (RSSR'), adsorption of asymmetric dialkylsulfides (RSR'), and co adsorption from thiol solutions (RSH+R'SH). The last cited technique was used as it gave a wider range of composition for mixed organic mercaptans: $CH_3(CH_2)_{11}SH$, $COOH(CH_2)_{11}SH$, $CH_2{=}CH\ (CH_2)_9\text{-}S\text{-}S\text{-}\ (CH_2)_9CH = CH_2$, and $OH(CH)_{11}SH$. These alkane thiols were chosen because of their identical alkane chain; only their functional group differs, so they have approximately the same length while having different hydrophobicities. These organic mercaptans assembled on the gold surface because of the energetically favorable Au-S bonds [15-23, 25]. The intermolecular interactions, such as Van Der Waals and H bonds cause the SAM to adopt a specific structural arrangement [64-69]. These interactions and the functionality groups also affect the density of coverage of the gold-coated substrate by SAM [66]. Surface of Si wafers were also coated with different silanes to vary their wettabilities as represented in Figure 1-3. Adsorption of silane was done on oxidized Si wafers through silane vapor deposition process.

The first part of this dissertation focuses on investigating the effects of organic mercaptans forming SAMs on gold to tailor the surface energy of the substrate, on the diblock copolymer rearrangements.

Diblock Copolymer and its Orientation in Thin Films

The second part of this dissertation describes the roughness-induced orientation of cylindrical domains in thin films of a polystyrene–poly(methylmethacrylate) diblock copolymer (PS-*b*-PMMA; 0.3 as the volume fraction of PMMA) shown in Figure 1-7. Atomic force microscopy (AFM) and cyclic voltammetry (CV) were used to assess the orientation of cylindrical PMMA domains in PS-*b*-PMMA films having different thicknesses (20-200 nm) on various substrates having different surface roughnesses and hydrophilicities. AFM was used to determine the orientation of PMMA domains at the free film surface. CV on gold substrates coated with PS-*b*-PMMA films whose PMMA domains were chemically removed, permitted us to determine the domain orientation at the polymer–substrate interface and also inside the film.

In a BCP film supported by a substrate, the orientation of cylindrical domains is strongly affected by interactions at the BCP–substrate interface and at the free surface of the BCP film. Preferential wetting of one fragment at an interface leads to horizontal domain orientation. To align cylindrical domains vertically to an underlying substrate, the substrate surface has often been chemically tailored to balance the wettability of the BCP fragments.[43, 44] For example, the appropriately tailored surfaces for PS-*b*-PMMA were obtained on hydrogen-terminated Si,[45] on substrates modified with organosilane self-assembled monolayers,[46] and on substrates covalently modified with a brush layer of a PS-PMMA random copolymer having an appropriate volume fraction.[43, 47] In addition to controlling the surface wettability of the underlying substrates, several approaches have been simultaneously employed to improve the vertical alignment of cylindrical PMMA domains in a PS-*b*-PMMA film, including optimization of film thickness,[34, 48] addition of PMMA homopolymers,[49] control of solvent-evaporation conditions,[50] and electric field application during annealing.[6, 10, 51] Russell et al. extensively utilized the

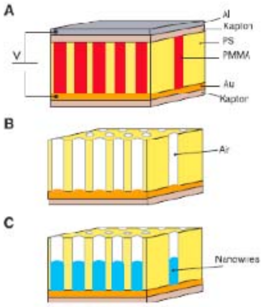

A schematic representation of high-density nanowire fabrication in a polymer matrix. (A) An asymmetric diblock copolymer annealed above the glass transition temperature of the copolymer between two electrodes under an applied electric field, forming a hexagonal array of cylinders oriented normal to the film surface. (B) After removal of the minor component, a nanoporous film is formed. (C) By electrodeposition, nanowires can be grown in the porous template, forming an array of nanowires in a polymer matrix.

Figure 1-2 Experimental Set-Up to Orient BCP Domains through Electric Field Application. [6]

application of electric field to induce the orientation of the BCP domains by using a set up shown in Figure 1-2.[6] By removing one of the BCP, Russell's group was able to grow nanowires within the pores. Kim and Nealey took advantage of organosilane coatings to change the surface wettability of the substrate as presented in Figure 1-3.[24] The obtained coatings led to a preference towards one of the BCP, allowing a specific orientation of the polymers within the film (Figure 1-8). Hydrophilic surfaces are wet by PMMA whereas hydrophobic ones preferentially attract PS. They reported that the domain orientation of the BCP followed the pattern made by the organosilane coatings on the substrate shown in Figure 1-9. Guarini and coworkers presented results, shown in Figure 1-6, demonstrated that the order of the domains in BCP films depends on the thickness of the film.[34]

Recently, Sivaniah and coworkers experimentally demonstrated that the roughness of a substrate surface induced the vertical alignment of lamellar PMMA microdomains in thin films of symmetric PS-*b*-PMMA (1:1).[52, 53] The domain orientation was influenced by the periodicity of the BCP domains, and the lateral periodicity and vertical amplitude of the surface corrugations of an underlying substrate. The BCP formed lamellar microdomains observed through cross-sectional transmission electron microscopy (TEM) as presented in Figure 1-4. The roughness-induced vertical alignment of BCP domains was theoretically explained using a model based on the distortion of aligned domain structures by the rough surface.[54-56] This model, shown is Figure 1-5, uses numerous assumptions, and the critical roughness for which the orientation transition is seen in BCP systems in contact with rough substrate still needs to be determined through more experiments.[56] The roughness-induced domain alignment provides a simple means for preparing PS-*b*-PMMA thin films containing vertically-aligned PMMA domains, because it does not require the chemical neutralization, where none of the blocks would preferentially wet the surface, of the substrate surface.[52, 53]

All these studies required difficult and time-consuming procedures. The intention here is to discover a more straightforward way to control the PMMA domains orientation in thin PS-*b*-PMMA films. Controlling the PS: PMMA ratio affects the type of PMMA domains. It is also possible to control the roughness by utilizing different types of substrates and/or modifying them to enlarge their grain size for instance. In this study, the effects of substrate surface roughness and hydrophilicity on the orientation of cylindrical PMMA domains in thin PS-*b*-PMMA films were investigated. AFM and CV were used to determine the orientation of cylindrical PMMA domains in PS-*b*-PMMA films having different thicknesses on different types of substrates.

The novelty of this work is the realization that a non-neutral rough substrate can be used to perpendicularly orient cylindrical nanodomains from symmetrical PS-*b*-PMMA without using neutral bounding surfaces.

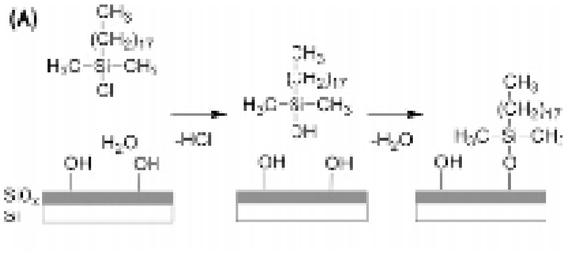

Figure 1-3 Scheme Representing an Organosilane Coating of Si Surface in Order to Control the Surface Wettability of the Substrate.

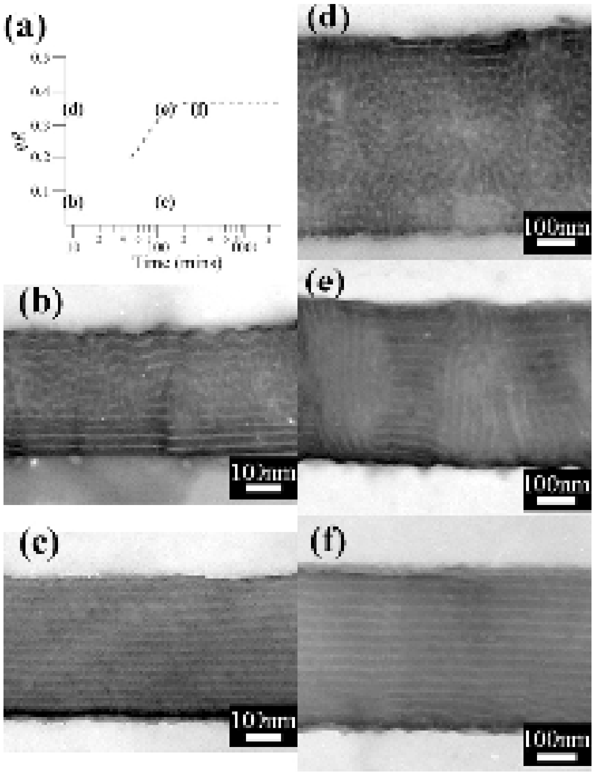

Figure 1-4 Cross-sectional TEM of 38K-36.8K PS-*b*-PMMA on S_ITO (b, c) and UC_ITO (d-f) substrates as a function of annealing time at 200 °C. Each of (b)-(f) is summarized in (a) in terms of their annealing time and ITO substrate roughness.[53]

Also shown in this figure is the locus of the crossover behavior as extracted from Figure 8 for 38K-36.8K PS-*b*-PMMA.

Where super critically rough ITO and under critically rough ITO are noted SC_ITO, and UC_ITO respectively.

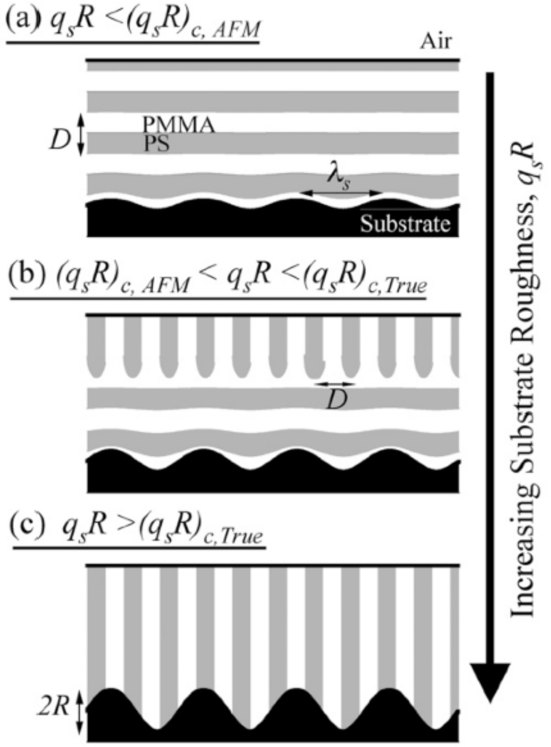

Figure 1-5 A schematic of the interior of block copolymer thin films (a) below the AFM observed critical substrate roughness, (qsR)c,AFM, (b) above (qsR)c,AFM, and (c) above the true critical substrate roughness, (qsR)c,true.[53]

The gray and unshaded areas refer to the PS and PMMA portions of the microdomain structure, respectively. The dark lines and black shaded areas refer to the air and substrate interfaces interfaces, respectively.

Where rough surface has a rough surface has a roughness of *q*s*R,* where *q*s ~ $2\pi/\lambda_s$. *R* is the (rootmean square) vertical displacement of the surface topography about a mean horizontal plane. λ_s is the characteristic lateral periodicity in the surface topography.

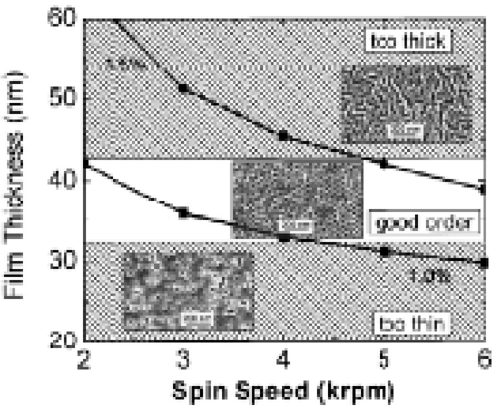

Figure 1-6 Ellipsometric film thickness as a function of spin speed for different concentration solutions of PS-PMMA diblock copolymer (*Mn* 567 000 g/mol) diluted in toluene ~percent by weight). [34]

Shaded regions indicate where film is too thin or too thick to achieve proper ordering of the polymer block domains. SEM images superimposed on the graph show representative film morphologies (after exposure and development) for the different film thicknesses.

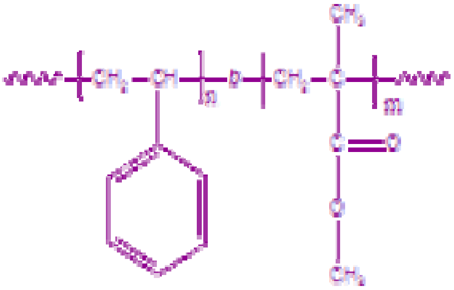

Figure 1-7 Structure of PS-*b*-PMMA Diblock Copolymer.

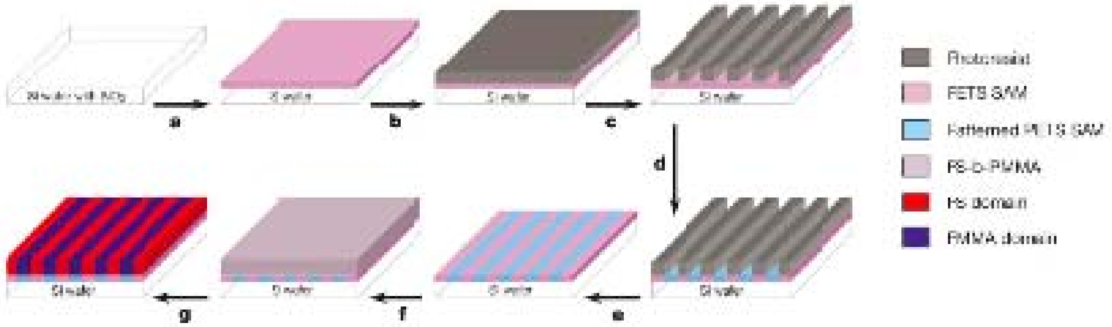

Figure 1-8 Schematic representation of the strategy used to create chemically nanopatterned surfaces and investigate the epitaxial assembly of block-copolymer domains. [24]

a, A SAM of PETS was deposited on a silicon wafer. b, Photoresist was spin-coated on the SAM-covered substrate, and c, patterned by extreme ultraviolet interferometric lithography (EUV-IL) with alternating lines and spaces of period Ls. d, The topographic pattern in the photoresist was converted to a chemical pattern on the surface of the SAM by irradiating the sample with soft X-rays in the presence of oxygen. e, The photoresist was then removed with repeated solvent washes. f, A symmetric, lamella-forming PS-b-PMMA copolymer of period Lo was spin-coated onto the patterned SAM surface and g, annealed, resulting in surface directed block-copolymer morphologies. Chemically modified regions of the surface presented polar groups containing oxygen and were preferentially wetted by the PMMA block, and unmodified regions exhibited neutral wetting behavior by the block copolymer.

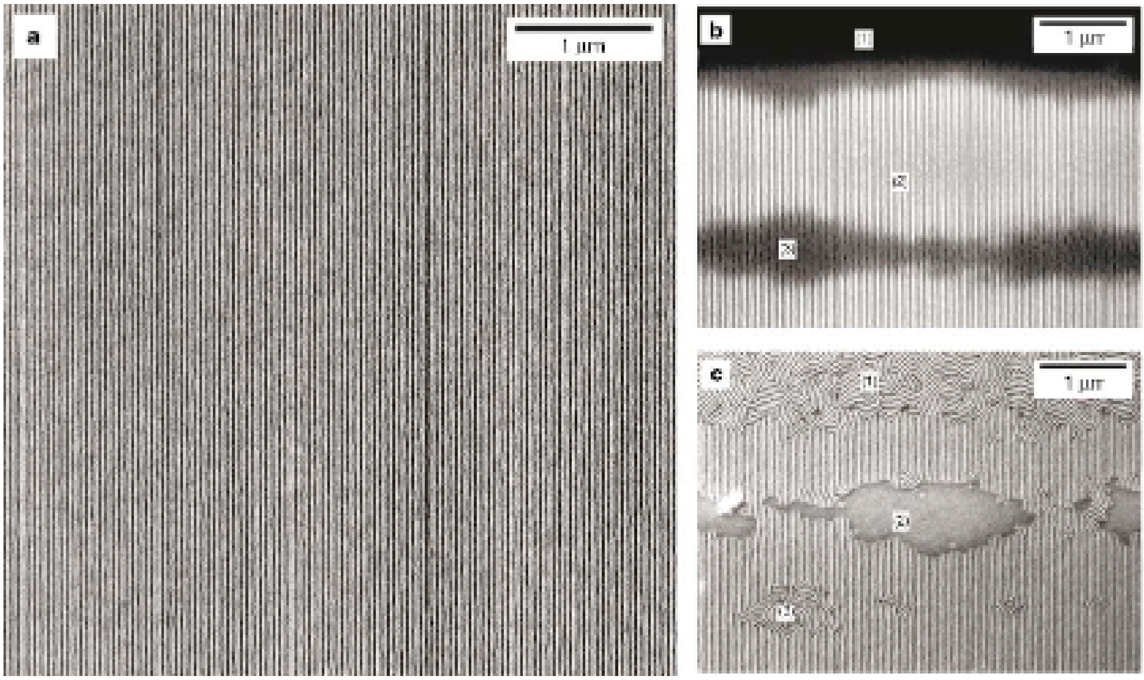

Figure 1-9 Top-down scanning electron microscopy (SEM) images of photoresist and PS-b-PMMA copolymer (Lo = 48 nm, film thickness of 60 nm) patterns. In the SEM images of the PS-b-PMMA copolymer the light and dark regions were PS and PMMA domains, respectively.[24]

a, The perfect epitaxial ordering of a block-copolymer pattern extended over a 5 mm by 5 mm area. In this case, the SAM surface was chemically patterned with a period of Ls = 47.5 nm that matched Lo. b, Top-down SEM image of the photoresist pattern (Ls = 47.5 nm) at the edge of the region exposed using EUV-IL, and c, top-down SEM image of the morphology of a block-copolymer film overlying a chemically nanopatterned surface that was prepared (as in Fig. 1-8) using a photoresist pattern similar to that shown in b. To allow for comparison between samples, the exposure doses during EUV-IL and chemical modification steps were controlled to within 2%. Regions (1), (2) and (3) in b delineate unpatterned, overexposed, and underexposed areas of the photoresist, respectively. Regions (1), (2) and (3) in c show the block-copolymer morphologies observed over corresponding areas. Lamellae were oriented perpendicularly without long-range order on the unpatterned (1) and underexposed (3) regions. In the overexposed (2) regions the lamellae adopted a morphology that was parallel to the surface.

References

1. Lazzari, M.; Lopez-Quintele, M. A. *Adv. Mater.* **2003**, *15*, 1583.
2. Krausch, G.: Magerle, R. *Adv. Mater.* **2002**, *14*, 1579.
3. Macromolecular Nomenclature for Stereochemical Definitions Related to Polymers *Pure and Appl. Chem.* **1981**, *53,* 733.
4. Jeong, U.; Ryu, D. Y.; Kim, J. K.; Kim, D. H.; Russell, T. P.; Hawker, C. J. *Adv. Mater.* **2003**, *15*, 1247.
5. Park, M.; Harrison, C.; Chaikin, P. M.; Register, R. A.; Adamson, D. H. *Science* **1997**, *276*, 1401.
6. Thurn-Albrecht, T. et al. *Science* **2000**, *290*, 2126.
7. Lopes, W. A.; Jaeger, H. M. *Nature* **2001***, 414*, 735.
8. Chan, V. Z. H. et al. *Science* **1999**, *286*, 1716.
9. Bates, F. S. Fedrickson, G. H. *Annu. Rev. Phys. Chem.* **1990**, *41*, 525.
10. Thurn-Albrecht, T.; Steiner, R.; DeRouchey, J.; Stafford, C. M.; Huang, E.; Bal, M.; Tuominen, M.; Hawker, C. J.; Russell, T. P. *Adv. Mater.* **2000**, *12*, 787.
11. Huang, E.; Rockford, L.; Russell, T. P.; Hawker, C. J.; Mays, J. *Nature* **1998**, *395*, 757.
12. Russell T. P. et al. *Macromolecules* **1998**, *31*, 8509.
13. Zalusky, A. S.; Olayo-Valles, R.; Taylor, C. J.; Hillmayer, M. A. *J. Am. Chem. Soc.* **2001**, *123*, 1519.
14. Adamson, A. W.: Gast, A. P. Physical Chemistry of Surfaces, 6th ed., Wiley-Interscience: New York, **1997.**
15. Poirier, G. E.; Pylant, E. D. *Science* (*Washington D.C.*) **1996**, *272*, 1145.
16. Nuzzo, R. G.; Allara, D. L. *J. Am. Chem. Soc.* **1983**, *105*, 4481.
17. Porter, M. D.; Bright, T. D.; Allara, D. L.; Chidsey, C. E. D. *J. Am. Chem. Soc.* **1987**, *109*, 3449.
18. Dubois, L. H.; Nuzzo, R. G. *Annu. Rev. Phys. Chem.* **1992**, *43*, 437.
19. Bain, C. D.; Evall, J.; Whitesides, G. M. *J. Am. Chem. Soc.* **1989**, *111*, 7155.
20. Bain, C. D.; Whitesides, G. M. *Science (Washington, D.C.)* **1988**, *240*, 62.

21. Biebuyck, H. A.; Bain, C. D.; Whitesides, G. M. *Langmuir* **1994**, *10*, 1825.
22. Laibinis, P.E .; Whitesides, G. M.; Allara, D. L.; Tao, Y. T.; Parikh, A. N.; Nuzzo, R. G. *J. Am. Chem. Soc.* **1991**, *113*, 7152.
23. Dubois, L. H.; Zegarski, B. R.; Nuzzo, R. G. *J. Chem. Phys.* **1993**, *98*, 678.
24. Kim, S. O.; Solak, H. H.; Stoykovich, M. P.; Ferrier, N. J.; De Pablo, J. J.; Nealey, P. F. *Nature* **2003**, *424*, 411.
25. Patai, S.; Rappoport, Z. *The Chemistry of Organic Derivatives of Gold and Silver* Wiley and Sons Ltd **1999.**
26. Ito, T. *Journal of Electroanalytical Chemistry* **2001**, *495*, 87.
27. Czaplewski, K. F.; Hupp, J. T.; Snurr, R. Q. *Adv. Mater.* **2001**, *13*, 1895.
28. Lee, S. B.; Mitchell, D. T.; Trofin, L.; Nevanen, T. K.; Sodeslund, H.; Martin, C. R. *Science* **2002**, *296*, 2198.
29. Chun, K. Y.; Stroeve, P. *Langmuir* **2002**, *18*, 4653.
30. Kholi, P.; Harrell, C. C.; Cao, Z.; Tan, W.; Martin, C. R. *Science* **2004**, *305*, 984.
31. Gyurcsany, R. E.; Vigassy, T.; Pretsch, E. *Chem. Commun.* **2003**, 2560.
32. Kim, H. C.; Jia, X.; Stafford, C. M.; Kim, D. H.; McCarthy, T. J.; Tuominen, M.; Hawker, C. J.; Russel, T. P. *Adv. Mater.* **2001**, *13*, 795.
33. Crossland, E. J. W.; Ludwigs, S.; Hillmyer, M. A.; Steiner, U. *Soft Matter* **2007**, *3*, 94.
34. Guarini, K. W.; Black, C. T.; Milkove, K. R.; Sandstrom, R. L. *J. Vac. Sci. B* **2001**, *19*, 2784.
35. Yang, S. Y.; Ryu, I.; Kim, H. Y.; Kim, J. K.; Jang, S. K.; Russell, T. P. *Adv. Mater.* **2006**, *18*, 709.
36. Zhang, Q.; Xu, T.; Butterfield, D.; Misner, M. J.; Ryu, D. Y.; Emrick, T.; Russell, T. P. *Nano Lett.* **2005**, *5*, 357.
37. Fasolka, M. J.; Mayes, A. M. *Annu. Rev. Mater. Res.* **2001**, *31*, 323.
38. Li, M.; Coenjarts, C. A.; Ober, C. K. *Adv. Polym. Sci.* **2005**, *190*, 183.
39. Hillmyer, M. A. *Adv. Polym. Sci.* **2005**, *190*, 137.
40. Olson, D. A.; Chen, L.; Hillmyer, M. A. *Chem. Mater.* **2008**, *20*, 869.
41. Park, M.; Harrison, C.; Chaikin, P. M.; Register, R. A.; Adamson, D. H. *Science* **1997**, *276*, 1401.

42. Darling, S. B.; Yufa, N. A.; Cisse, A. L.; Bader, S. D.; Sibener, S. J. *Adv. Mater.* **2005**, *17*, 2446.
43. Mansky, P.; Russell, T. P.; Hawker, C. J.; Pitsikalis, M.; Mays, J. *Macromolecules* **1997**, *30*, 6810.
44. Huang, E.; Russell, T. P.; Harrison, C.; Chaikin, P. M.; Register, R. A.; Hawker, C. J.; Mays, J. *Macromolecules* **1998**, *31*, 7641.
45. Xu, T.; Kim, H.-C.; DeRouchey, J.; Seney, C.; Levesque, C.; Martin, P.; Stafford, C. M.; Russell, T. P. *Polymer* **2001**, *42*, 9091.
46. Niemz, A.; Bandyopadhyay, K.; Tan, E.; Cha, K.; Baker, S. M. *Langmuir* **2006**, *22*, 11092.
47. Mansky, P.; Liu, Y.; Huang, E.; Russell, T. P.; Hawker, C. *Science* **1997**, *275*, 1458.
48. Fasolka, M. J.; Banerjee, P.; Mayes, A. M.; Pickett, G.; Balazs, A. C. *Macromolecules* **2000**, *33*, 5702.
49. Jeong, U.; Ryu, D. Y.; Kho, D. H.; Kim, J. K.; Goldbach, J. T.; Kim, D. H.; Russell, T. P. *Adv. Mater.* **2004**, *16*, 533.
50. Xuan, Y.; Peng, J.; Cui, L.; Wang, H.; Li, B.; Han, Y. *Macromolecules* **2004**, *37*, 7301.
51. Thurn-Albrecht, T.; DeRouchey, J.; Russell, T. P.; Jaeger, H. M. *Macromolecules* **2000**, *33*, 3250.
52. Sivaniah, E.; Hayashi, Y.; Iino, M.; Hashimoto, T.; Fukunaga, K. *Macromolecules* **2003**, *36*, 5894.
53. Sivaniah, E.; Hayashi, Y.; Matsubara, S.; Kiyono, S.; Hashimoto, T.; Fukunaga, K.; Kramer, E. J.; Mates, T. *Macromolecules* **2005**, *38*, 1837.
54. Podariu, I.; Chakrabarti, A. *J. Chem. Phys.* **2000**, *113*, 6423.
55. Tsori, Y.; Andelman, D. *Macromolecules* **2003**, *36*, 8560.
56. Tsori, Y.; Sivaniah, E.; Andelman, D.; Hashimoto, T. *Macromolecules* **2005**, *38*, 7193.
57. Ito, T.; Audi, A. A.; Dible, G. P. *Anal. Chem.* **2006**, *78*, 7048.
58. Bond, A. M.; Luscombe, D.; Oldham, K. B.; Zoski, C. G. *J. Electroanal. Chem.* **1988**, *249*, 1.

59. Brandini, P.; Stroeve, P. *Macromolecules* **2003**, *36*, 9502.
60. Whitesides, G. M.; Laibinis, P. E. *Langmuir* **1990**, *6*, 87.
61. Laibinis, P. E.; Fox, M. A.; Folkers, J. P.; Whitesides, G. M. *Langmuir* **1991**, *7*, 3167.
62. Brandini, P.; Stroeve, P. *Macromolecules* **2003**, *36*, 9492.
63. Lay, M. D.; Varazo, K.; Stickney, J. L. *Langmuir* **2003**, *19*, 8416.
64. Dannenberger, O.; Wolff, J. J.; Buck, M. *Langmuir* **1998**, *14*, 4679.
65. Yamada, R.; Sakai, H.; Uosaki, K. *Chem. Lett.* **1999**, 667.
66. Ishida, T.; Mizutani, W.; Azehera, H.; Sato, F.; Choi, N.; Akiba, U.; Fujihara, M.; Tokumoto, H. *Langmuir* **2001**, *17*, 7459.
67. Kawasaki, M.; Sato, T.; Tanaka, T.; Takao, K. *Langmuir* **2000**, *16*, 1719.
68. Yamada, R.; Wano, H.; Uosaki, K. *Langmuir* **2000**, *16*, 5523.
69. Rai, B.; Sathish, P.; Malhotra, C. P.; Pradip, Ayappa, K. G. *Langmuir* **2004**, *20*, 3138.

CHAPTER 2 - Analytical Techniques Used in the Research

Introduction

The creation of the samples involves at least four steps, namely: cleaning the substrates, films spin casting, samples annealing, and PMMA removal. In Chapter 3, the use of SAMs adds an extra step: SAM coating of the substrates. In this research, major analytical techniques were used to define the properties and characteristics of the samples at each stage of the procedure, that is goniometry, spectroscopic ellipsometry, atomic force microscopy, and cyclic voltammetry. Each technique has a specific role and questions to answer. Goniometry permitted to check the cleanliness of the substrate as well as the coverage of its surface with SAMs. Spectroscopic ellipsometry was used to measure film thicknesses whether it was SAM or PS-*b*-PMMA. Atomic force microscopy showed topographic images of the plain substrates, and BCP films after spin casting, annealing, and PMMA removal. Cyclic Voltammetry was used to investigate the extent of PMMA removal as well as the orientation of the pores in the PS matrix.

Goniometry [1, 2, 3, 4]

A goniometer, from the Greek “gonia” meaning angle and “metron” meaning measure, is an instrument that measures angles. It is commonly used in surface science to measure static contact angle, advancing and receding angle, and surface tension. Here, this technique was utilized to measure static contact angle. This angle is formed by a liquid, here pure water, at the three phase boundary where liquid, gas, and solid intersect as shown in Figure 2-1. The contact angle θ depends on the interfacial tensions between the liquid/solid (γ_{SL}), the gas/solid (γ_{SG}), and the liquid/gas (γ_{LG}). It is possible to analytically express the contact angle with Young’s Relation see Equation 2-1.

$\gamma_{SG} = \gamma_{SL} + \gamma_{LG} \cos \theta$ Equation 2-1

It is assumed that the droplet fits the geometry of a sphere. The goniometer measures this contact angle θ. θ directly provides information on the interaction energy between surface and liquid. IT can be described in term of adhesion vs. cohesion. Adhesion is the

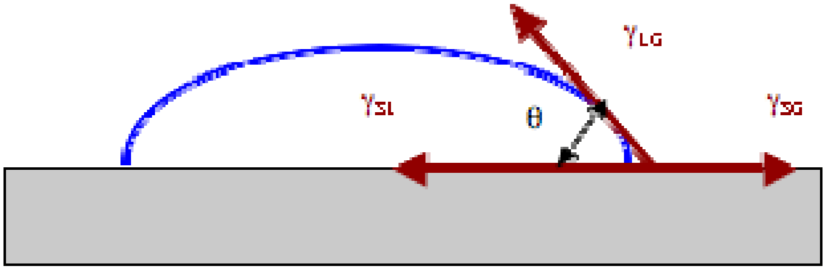

Figure 2-1 Contact angle θ of a Liquid Sample Fitting Young Equation.

force between the liquid molecules and the solid molecules. Cohesion is the force between the liquid molecules that hold the liquid together. Therefore, θ is the quantitative measure telling the goniometer user the ratio of cohesion vs. adhesion. If $\theta \sim 0$ denotes the adhesive forces are dominating, so the droplet spread completely on the solid surface. If θ is very high, cohesive forces are dominating, so the droplet beads up on the solid surface. It takes energy to do that. It comes from the surface of the solid; forces that hold the molecules of the solid together. Forces of attraction between polar molecules are stronger than those between non polar. So they are sufficiently strong to overcome the surface tension forces of the water and cause the droplet to form a film. Low energy surface, for instance hydrocarbon molecules, have weak forces. Consequently, polar liquid, such as water tend to form droplets on the surface rather than spread out.

It is challenging to coat low energy surfaces, but there are ways to converting these surfaces into high energy surfaces. All the ways aim to form oxygen-containing species at the surface. This kind of oxidation can be achieved by UV exposure, plasma or acid treatment. These methods were used in this research.

Surface energy quantifies the disruption of intermolecular bonds that occurs when a surface is created. Surface energy is defined as the excess energy at the surface o a material compared to the bulk.[1] Because the measurement of θ involves the consideration of the behavior of liquid in contact with solids and formation of droplets or thin films, it is referred to as surface energy measurement.

Spectroscopic Ellipsometry [5, 6, 7]

The name "ellipsometry" stems from the fact that the most general state of polarization is elliptic. Spectroscopic ellipsometry is s very sensitive measurement technique. It provides capabilities for thin films metrology. As an optical technique, spectroscopy ellipsometry is non-destructive and contact less.

Upon the analysis of the change of polarization of light, which is reflected off a sample, ellipsometry can yield information about layers that are thinner than the wavelength of the probing light itself. Ellipsometry measures the change of polarization upon reflection. The nature of the polarization change is determined by the properties of the sample, namely: thickness, complex refractive index or dielectric function tensor.

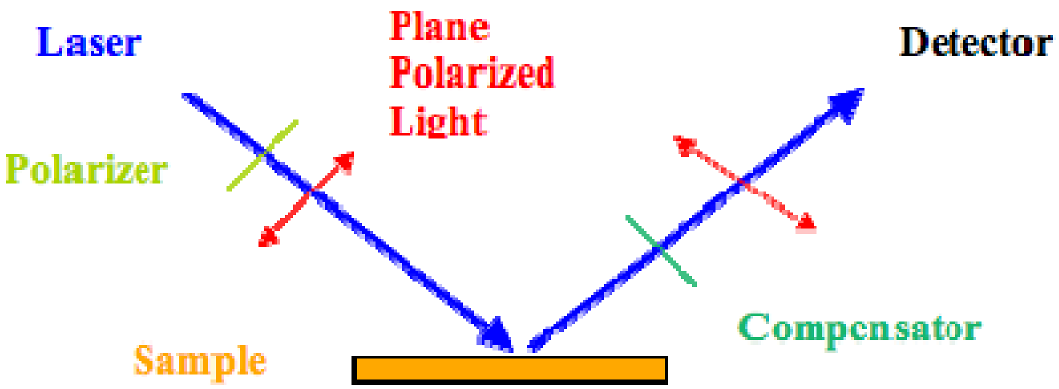

Figure 2-2 Basic Components of an Ellipsometer.

Ellipsometry measures two of the four Stokes parameters, which are Ψ and Δ. The polarization state of the light incident upon the sample is decomposed into an *s* and a *p* component. The *s* component is oscillating perpendicular to the plane of incidence and parallel to the sample surface. The *p* component is oscillating parallel to the plane of incidence. The amplitudes of the *s* and *p* components, after reflection and normalized to their initial value, are respectively denoted by *rs* and *rp*. Ellipsometry measures the ratio of *rs* and *rp*, which is described by the fundamental equation of ellipsometry as shown in Equation 2-2:

$$\rho = r_p / r_s = \tan(\Psi)e^{i\Delta} \quad \text{Equation 2-2.}$$

Where Δ is the phase shift, and Ψ the amplitude ration upon reflection.

A layer model must be established, which considers the optical constant such as refractive index, and thickness parameters of all individual layers of the sample including the correct layer sequence. Using an iterative procedure (least-squares minimization) unknown optical constants and/or thickness parameters are varied, and Ψ and Δ values are calculated. The calculated values of Ψ and Δ matching the experimental data best provide the optical constants and thickness parameters of the sample.

It is commonly used to characterize film thicknesses for simple layers or complex multilayer stacks ranging from few nanometers to several micrometers with a high accuracy. Figure 2-2 presents the basic components of an ellipsometer.

Atomic Force Microscopy [8, 9]

The atomic force microscope (AFM) is a very high-resolution type of scanning probe microscope, with resolution of fractions of a nanometer. The term “microscope” in the name is not accurate as it implies looking, while in fact the information is gathered by "feeling" the surface with a mechanical probe. Piezoelectric elements that facilitate tiny but precise movements on command enable the highly precise scanning. Figure 2-3 presents the basic components of an AFM. Additionally, samples viewed by AFM do not require any special treatments that would irreversibly change or damage the sample.

The AFM consists of a micro scale cantilever with a sharp tip, called probe, at its end that is used to scan the sample surface. Typically, the cantilever is made of silicon or silicon nitride. Its tip radius of curvature is on the order of nanometers. When the tip is brought into proximity of a sample surface, forces between the tip and the sample lead to a deflection of the cantilever according to Hooke's law shown in Equation 2-3.

$$F = -k\,x \qquad \text{Equation 2-3.}$$

Where x is the distance that the spring has been stretched or compressed away from the equilibrium position, F is the restoring force exerted by the material, and k is the force constant or spring constant.

Depending on the situation, forces that are measured in AFM include mechanical contact force, Van der Waals forces, capillary forces, chemical bonding, electrostatic forces, etc. Typically, the deflection is measured using a laser spot reflected from the top surface of the cantilever into an array of photodiodes. A feedback mechanism is employed to adjust the tip-to-sample distance to maintain a constant force between the tip and the sample. The sample is mounted on a piezoelectric tube that can move the sample in the z direction for maintaining a constant force, and the x and y directions for scanning the sample.

Depending on the application, the AFM can be operated on different modes, namely Contact Mode, Tapping Mode, Phase Imaging. For this research, the Tapping Mode was used.

In Tapping Mode, the cantilever is driven to oscillate up and down at near its resonance frequency. When the tip comes close to the surface, forces such as Van der Waals force or dipole-dipole interaction, electrostatic forces, …etc, act on the cantilever and cause the amplitude of the oscillation to decrease as the tip gets closer to the sample. The piezoelectric controls the height of the cantilever above the sample. The height is adjusted to maintain a set cantilever oscillation amplitude as the cantilever is scanned over the sample. Therefore, a Tapping AFM image is produced by imaging the force of the oscillating contacts of the tip with the sample surface.

The AFM was used in the research to provide a true three-dimensional surface profile of the sample at different stage of its fabrication to determine the roughness of the plain substrate, the topography and domain arrangement of PS-*b*-PMMA films before and after annealing, and after PMMA removal.

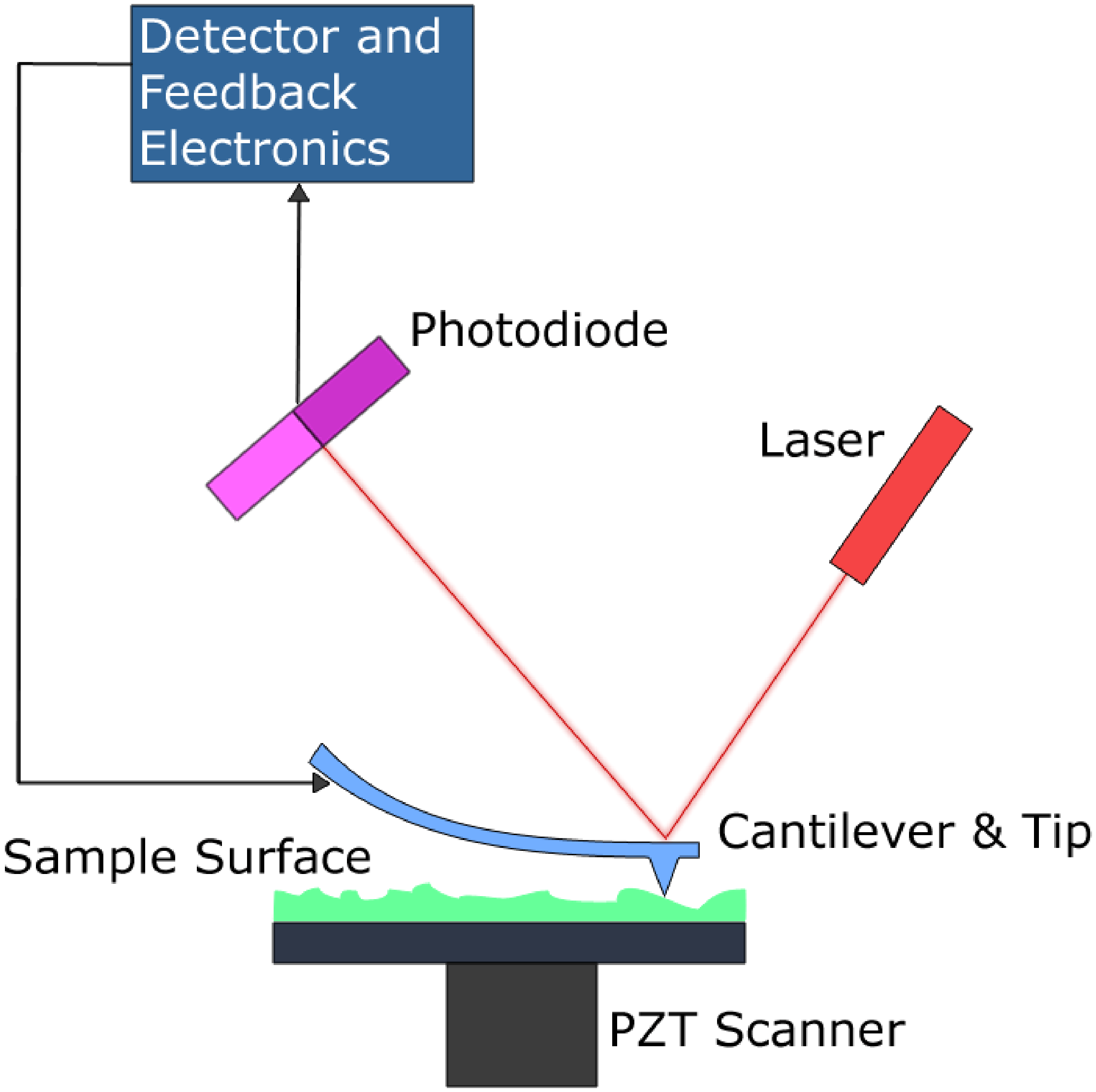

Figure 2-3 Basic Components of an AFM.

Cyclic Voltammetry [10, 11]

Cyclic voltammetry (CV) is a type of potentiodynamic electrochemical measurement. Cyclic voltammetry is generally used to study the electrochemical properties of an analyte in solution. A typical cyclic voltammogram is shown in Figure 2-4. The method uses a reference electrode, a working electrode, and a counter electrode referred to as a three-electrode setup as shown in Figure 2-5. Electrolyte is usually added to the test solution to ensure sufficient conductivity. The combination of the solvent, electrolyte and specific working electrode material determines the range of the potential.

In cyclic voltammetry, the electrode potential ramps linearly versus time. The potential is measured between the reference electrode and the working electrode. The current is measured between the working electrode and the counter electrode. This data is then plotted as current (i) vs. potential (E). The scan produces a current peak for any analytes that can be reduced (or oxidized depending on the initial scan direction) through the range of the potential scanned. The current increases as the potential reaches the reduction potential of the analyte, but then decreases as the concentration of the analyte is depleted close to the electrode surface. When the redox couple is reversible, the applied potential is reversed; it reaches the potential that re-oxidizes the product formed in the first reduction reaction. Therefore, it produces a current of reverse polarity from the forward scan. This oxidation peak usually has a similar shape to the reduction peak. As a result, information about the redox potential and electrochemical reaction rates of the compounds are obtained.

Depending of the scan rate, the shape of the peak changes (shown in Figure 5-4). The transition from the linear to radial diffusion modes reflects the change in scan rate. At fast scan rate, a linear diffusion of the redox molecules within the pores is observed as represented in Figure 2-6a, leading to peak shaped CVs. The peak current is determined through Equation 2-4:

$$I_p = 0.466nFAC\,(nFD\upsilon/RT)^{1/2} \qquad \text{Equation 2-4.}$$

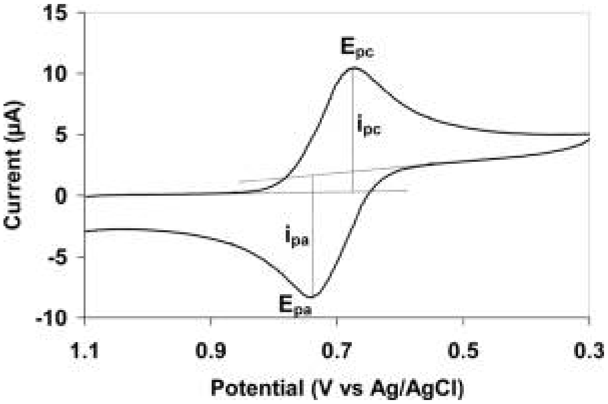

Figure 2-4 Typical Cyclo Voltammogram. [10]

i_{pa}: peak of the anodic current, i_{pc}: peak of the cathodic current, E_{pa} and E_{pa}: peak potentials.

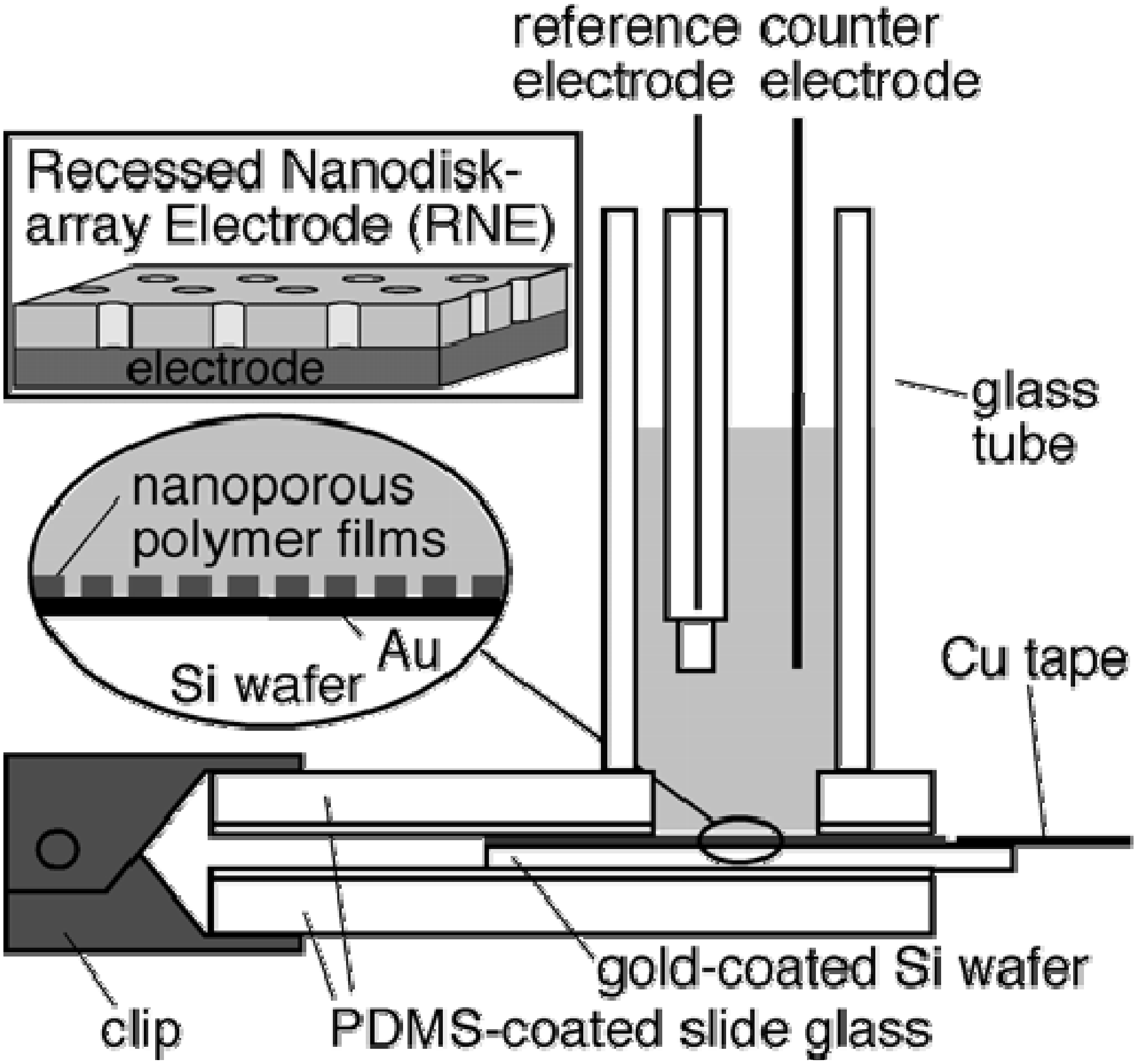

Figure 2-5 Three Electrodes set-up. [12]

Three-Electrode Cell Containing a Ag/AgCl (3 M KCl) Reference Electrode a Pt Counter Electrode, and a RNE Working Electrode.

where *n* is the number of electrons, *F* is Faraday's constant (96485 C/mol), *R* is the gas constant (8.31 J/K mol), *T* is temperature (298 K), *A* is the electrode area [$N\pi a^2$; *a* is the average radius of nanopores; *N* is the number of exposed nanopores], *D* is the diffusion coefficient of the redox-active, and *C* (mol/cm^3) is its concentration.

At slower scan rate, a radial diffusion of the redox molecules from outside the pores is observed as represented in Figure 2-6b, leading to sigmoidal shaped CVs. In this case, the limiting current is determined through Equation 2-5:

$I_{lim} = (4\pi n FCDa^2N)/(4L+\pi a)$ Equation 2-5.

where *n* is the number of electrons, *F* is Faraday's constant (96485 C/mol), *A* is the electrode area [$N\pi a^2$; *a* is the average radius of nanopores; *N* is the number of exposed nanopores], *D* is the diffusion coefficient of the redox-active, *C* (mol/cm^3) is its concentration, and L the channels length.

At very slow scan rate, the individual radial diffusion overlap and lead to a linear diffusion over all as represented in Figure 2-6c.

In this research, Cyclic Voltammetry was used to investigate the extent of PMMA removal as well as the orientation of the pores in the PS matrix.

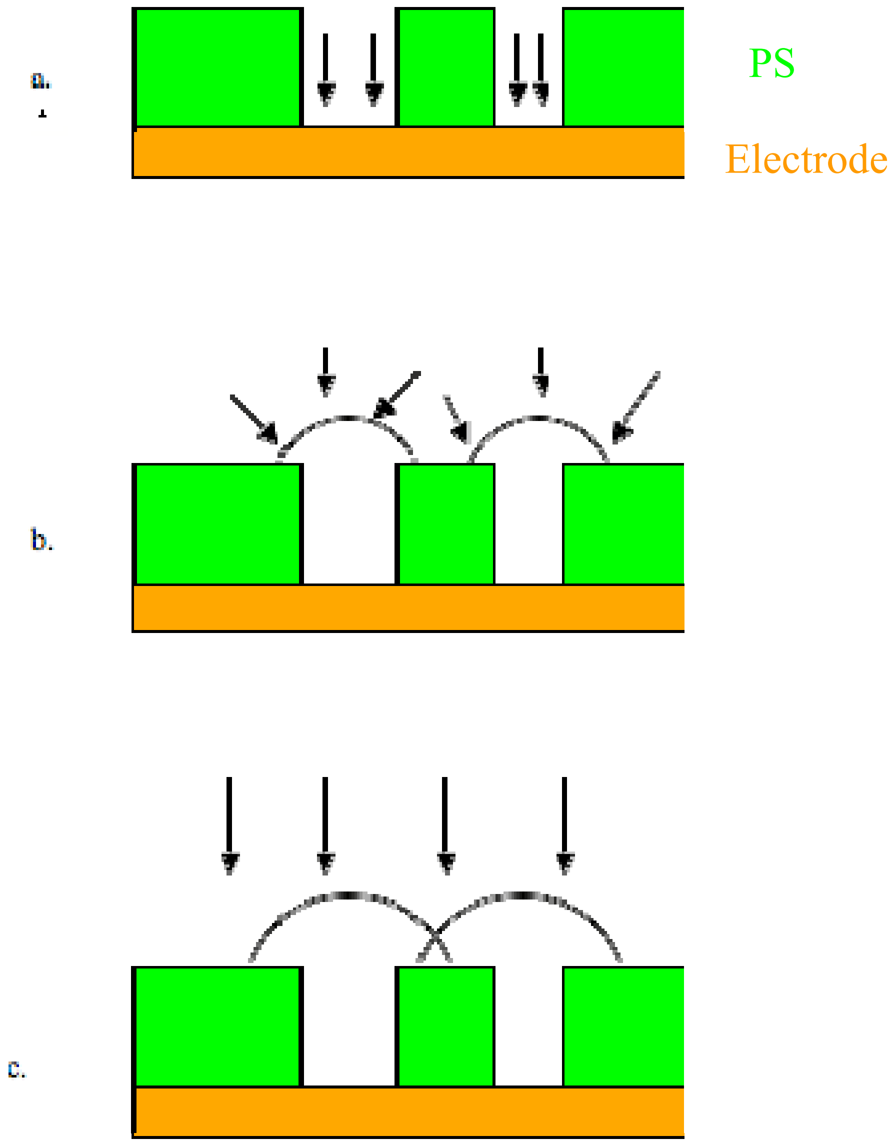

Figure 2-6 Representation of the Change in Diffusion Depending on the Scan Rate: a. Fast Scan Rate: Linear Diffusion, b. Slower Scan Rate: Radial Diffusion, c. Very Slow Scan Rate: Linear Diffusion.

References

1. Tadmor, R., *Langmuir* **2004**, *20*, 7659-7664.
2. De Gennes, P.G., *Reviews of Modern Physics* **1985**, *57*, 3, 827-863.
3. Isrealachvili, J., *Intermolecular and Surfaces*, Academic Press (1985-2004)
4. Young T. (1805) "An Essay on the Cohesion of Fluids" *Phil. Trans. R. Soc. Lond. 95: 65-87.*
5. Azzam, R. M. A.; Bashara, N. M., *Ellipsometry and Polarized Light*, Elsevier Science Pub Co (1987)
6. H. G. Tompkins and E. A. Irene (Editors), *Handbook of Ellipsometry* William Andrews Publications, Norwich, NY **2005**.
7. Fujiwara, H. *Spectroscopic Ellipsometry: Principles and Applications*, John Wiley & Sons Inc **2007.**
8. Humphris, A. D. L.; Miles, M. J., Hobbs J. K., *Applied Physics Letters*, **2005**, *86*, 034106 .
9. Giessibl F., *Advances in Atomic Force Microscopy, Reviews of Modern Physics*, **2003**, 75 (3), 949-983.
10. Bard, A.J.; Faulkner, L.R. Electrochemical Methods: Fundamentals and Applications. New York: John Wiley & Sons, 2nd Edition, **2001**.
11. Ito, T.; Audi, A. A.; Dible, G. P. *Anal. Chem.* **2006**, *78*, 7048-7053.
12. Li, Y.; Maire, H. C.; Ito, T. *Langmuir* **2007**, *23*, 12771.

CHAPTER 3 - Diblock Copolymer Orientation via SAM Treated Substrates

Introduction

SAMs are made of molecular constituents that spontaneously assemble onto the surface of solids [15-59]. It is easy to prepare, stable in electrolyte solution meaning that it is excellent for electrochemical sensors, and as it will be discussed useful for the fabrication of nanometer-scale structures. Figure 3-1 shows the generic structure of organic mercaptans used to synthesize films having specific compositions. The functional group can be changed as needed [5, 6]; therefore it is possible to tailor the properties of SAMs, such as wettability, surface energy, surface chemistry [4-6, 11, 18, 23, 24]. A chemical functionality sits at the head group of SAM. Oxidative adsorption leads to a metal-sulfur bond as shown in Equation 1.

Equation 1. $Au + RS^{-} \leftrightarrow Au\text{-}SR + e^{-}$

A simple sulfur ad-layer will then be formed on gold [19]. Therefore, it forms a flexible, well-defined film as shown in Figure 3-1, having the capacity to be simply tailored in order to vary the interfacial properties of the substrate [4-6, 11, 18, 23, 24]. The molecular components of SAM are responsible for its flexibility, and its thickness. Generally, the range of thickness of a SAM film is 1 to 3 nm, and is dependent on the length of the alkane chain.

There exist various types of thiols that can be used to form SAMs on the substrate having different sizes and shapes. Choosing the appropriate thiols is crucial to achieve the suitable conditions, such as wettability of the substrate, to go on with the experiment.

The goal here is to incorporate a specific molecular species in SAM in order to reach the same new property continuously all over the surface of the substrate [11, 25]. In other words, different n-alkane thiols are mixed to obtain a suitable wettability of the gold-coated wafer. Depending on the length of the alkane chain as well as the functional

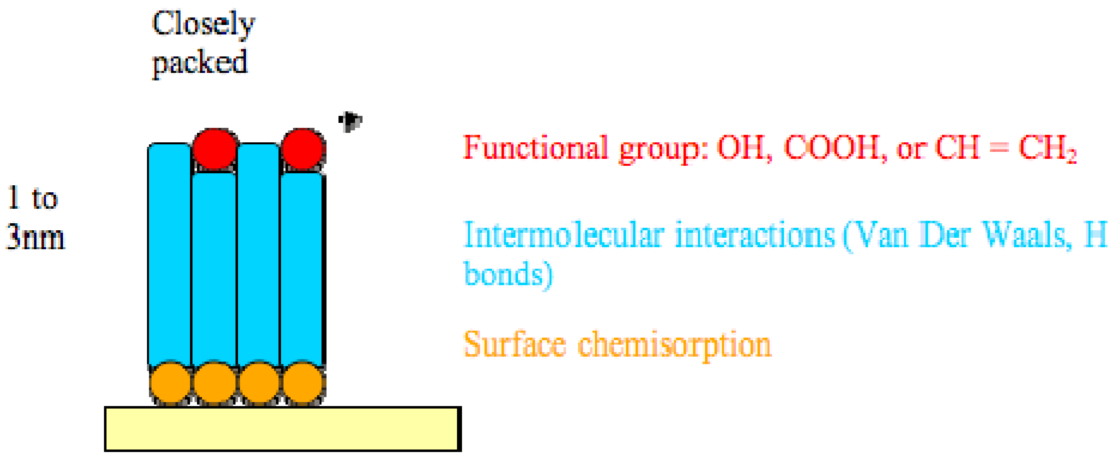

Figure 3-1 Representation of SAM. Deposited onto Gold-Coated Wafer Surface.

group, the properties of a thiol vary [4-6, 11, 18, 23, 24]. For instance, for an alkane thiol the longer the alkane chain the greater the hydrophobicity; on the contrary a hydroxyl group would increase the hydrophilicity of the SAM. This change in hydrophilicities leads to a change of surface properties thought to be accountable for the orientation of BCPs domains. Our goal was to observe how the domains of BCPs would orient depending on the surface properties of the substrate.

There are three ways to mix organic mercaptans [26]: adsorption of asymmetric disulfides (RSSR'), adsorption of asymmetric dialkylsulfides (RSR'), and co adsorption from thiol solutions (RSH+R'SH). The last cited technique was used as it gives a wider range of composition for mixed organic mercaptans: $CH_3(CH_2)_{11}SH$, $COOH(CH_2)_{11}SH$, $CH_2=CH\ (CH_2)_9$-S-S- $(CH_2)_9CH = CH_2$, and $OH(CH)_{11}SH$. These alkane thiols were chosen because of their identical alkane chain; only their functional group differs, so they have approximately the same length while having different hydrophobicity. These organic mercaptans assemble on the gold surface because of the energetically favorable Au-S bonds [1-9, 26]. The intermolecular interactions, such as Van Der Waals and H bonds cause the film to adopt a specific structural arrangement [13-17, 21]. These interactions and the functionality groups also affect the density of coverage of the gold-coated substrate by SAM [15]. SAMs are dynamic systems [13-17, 21]where reconstruction occurs due to environmental response, lateral diffusion, coverage driven ordering transitions, and conformational isomerism [13-16]. The entire dynamics in the molecular level structure of SAMs lead to macroscopic interfacial phenomena.

In this chapter, the effects of substrate hydrophilicity on the orientation of cylindrical PMMA domains in thin films of asymmetric PS-*b*-PMMA were studied. Organic mercaptans forming SAM on gold were used to tailor the surface energy of the substrate in order to investigate their effect on the diblock copolymer rearrangement. AFM was used to verify the orientation of cylindrical PMMA domains in PS-*b*-PMMA films deposited onto substrates having different hydrophilicities.

Experimental

Chemicals

PS-*b*-PMMA (Average molecular weight of PS and PMMA: respectively 39,800 and 17,000; polydispersity: 1.06) was purchased from Polymer Source Inc., and used as received. Toluene (Fischer Chemical), ethanol, 11- Mercaptoundecanoic Acid (Aldrich), 11-Mercapto-1-undecanol (Aldrich), 1-Dodecanethiol 98% (Acros) were used without any further purification. $CH_2=CH\ (CH_2)_9\text{-S-S-}\ (CH_2)_9CH = CH_2$ was synthesized by Feng Li in Ito's laboratory.

Substrates

Gold-coated silicon wafers (Au-Si), which were prepared via sputtering 10 nm Ti followed by 200 nm Au onto Si (100) wafers, were purchased from LGA Thin Films (Foster City, CA).

Cleaning Substrates

All substrates were sonicated in ethanol for 10 minutes, dried with argon, and then cleaned in a Novascan PSD-UVT UV-Ozone system for 30 minutes prior to be used.

Preparation of SAM

The gold-coated wafer was treated right after the last step of its cleansing procedure. The most common protocol to treat surfaces with alkane thiol is immersion of the substrate into 1mM ethanolic solution of thiols for 12 to 18 hours at room temperature [10-24, 26]. When used as a solvent to make SAM, ethanol gives better organized, densely packed SAM having less defects than SAM made of other solvents such as toluene, tetrahydrofuran, or acetonitrile [13, 14]. The temperature is another parameter that had also been studied [16, 17]. It has been shown that only during the first few minutes of dipping a temperature higher than 25°C would increase the kinetic of formation. As this protocol lasts many hours, it was done at room temperature. It has been proven that an increase of thiol concentration would result in a decrease in immersion time [12]. There again, as the immersion time is long, a small concentration such as 1mM was enough. Therefore the clean gold-coated wafers were dipped in an ethanolic mixed alkane thiol solution having various ratios leading to different surface energies. A dense coverage of the substrate occurred rapidly [13]; the longer the dipping, the higher the density of molecules and the

Table 3-1 Contact Angle Measurements of Gold-Coated Wafer After Various Treatments with Pure Thiols and Mixed at Different Ratios.

Sample [(a)]	Clean Au	Pure CH_3	Pure $CH_2{=}CH$	Pure COOH	Pure OH	1:3 CH_3/ COOH	1:3 $CH_2{=}CH$/ COOH	1:3 CH_3/OH	1:3 $CH_2{=}CH$/OH
θ^{water}	45-43	112-116	96-99	63-67	19-22	93-95	65-69	101-104	45-49

a) The type of thiol used to treat the gold-coated wafer surface is represented here only by its terminal functional group.

The concentrations of all solutions were 1mM. The gold-coated wafer treatment was done over night.

lower the defects in SAM [12]. The treatment was carried out over night, after that the sample was rinsed with ethanol, then dried with argon. Table 3-1 presents the contact angle measurements obtained after an over night dipping of the cleansed gold-coated wafer in 1mM mixed thiol solutions. A water droplet (2 μL) was placed onto a substrate surface, and the angles at the two opposite water-substrate interfaces were measured within 30 s after the drop deposition as shown in Figure 3-2. It also shows the results for plain clean gold (Au) as well as pure 1mM thiol solutions in order to be able to compare the results obtained for various thiols mix.

*Preparation of PS-*b*-PMMA Films*

Spin coating is an extensively used technique to cast films onto different types of substrates such as gold, and silicon [25, 28, 29, 30 -50]. It allows the researcher to control the thickness of the cast films by controlling the speed used. This technique leads to a better homogeneity of the film compared to dip coating, as well as a flatter surface. The treated wafers were flooded with the polymer toluene solution prior to spin up for 30 sec. The speed was varied as well as the polymer concentration until the targeted film thickness was reached.

Techniques

Characterization of SAM onto Gold-Coated Wafer

The thickness of SAM was measured using a J. A. Woollam alpha-SE spectroscopic ellipsometer.

The hydrophobicity of a substrate's surface was assessed by measuring water contact angles (θ^{water}) prior to depositing the polymer film. A water droplet (2 μL) was placed onto a substrate surface, and the angles at the two opposite water-substrate interfaces were measured within 30 s after the drop deposition as shown in Figure 3-2. Measurements were done in air with ultra-pure water.

AFM Measurements

AFM images were obtained by Tapping Mode imaging in air, using a Digital Instruments Multimode AFM with Nanoscope IIIa electronics. Probes for Tapping Mode

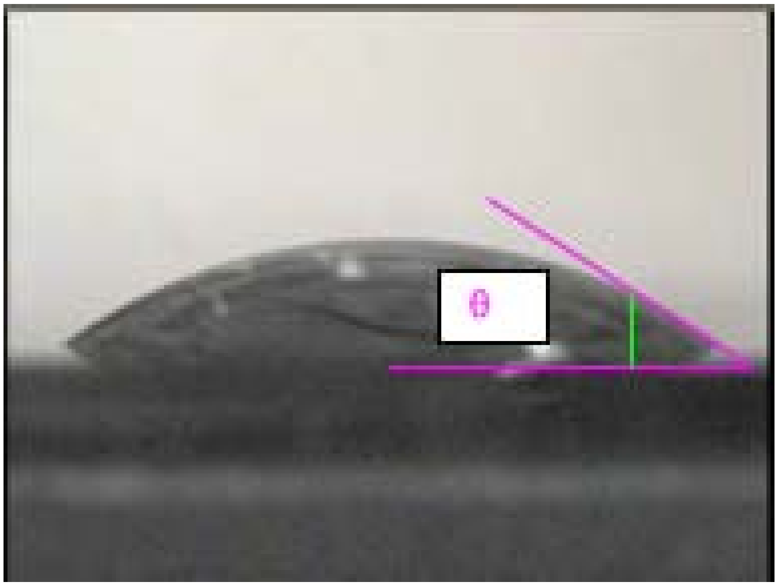

Figure 3-2 Picture of a 2 μL Water Droplet Deposited onto a Substrate Surface for Water Contact Angle Measurement Purpose.

This is an example showing how θ would be obtained.

AFM (cantilever length, 125 μm; force constant, 40 N/m; resonant frequency, 300 kHz) were purchased at Applied Nanostructures.

PS-b-*PMMA Films Thickness Measurements*

The thickness of PS-*b*-PMMA films was measured using a J. A. Woollam alpha-SE spectroscopic ellipsometer. Profiler, and spectroscopic ellipsometry [28] were used to measure the film thickness. Both profiler and spectroscopic ellipsometry gave similar results: the faster the spinning, the thinner the film. From these results, 0.7% weight concentration solutions were used and spin-casted at 2000 rpm onto the substrates.

Results and Discussion

Characterization of the SAM on Gold-Coated Wafer before PS-b-PMMA Films Deposition

Prior to the deposition of PS-*b*-PMMA films, the treated substrates surfaces were characterized using two different techniques: contact angle measurements [11, 26], and spectroscopic ellipsometry [3, 10, 27]. As SAM films are 1 to 3nm thick, its presence is detected through ellipsometric measurement, and its exact thickness is revealed. Table 3-1 presents the contact angle measurements of the surface of gold-coated wafers treated with a variety of mixed ethanolic solutions of different thiols. The values of θ^{water} obtained for pure SAM were fairly similar to the literature values; indeed, for $C_{12}H_{26}S$ the literature gave a θ^{water} of 105° [5], and the experiment revealed a θ^{water} of 112~116°. As expected, the mixture of hydrophobic organic mercaptan with a hydrophilic one (1:3 ratio), lead to an intermediate value of θ^{water}. For instance, a 1:3 ratio of $CH_2{=}CH\ (CH_2)_9$-S-S- $(CH_2)_9CH = CH_2$ (θ^{water}: 96~99): $OH(CH)_{11}SH$ (θ^{water}: 19~22), resulted of a SAM covered gold-coated wafer presenting a θ^{water}: 45~49.

To confirm the presence of SAMs on the surface of the treated substrates, ellipsometric measurements were taken, and are presented in Table 3-2. The thickness of different SAMs deposited onto the substrate surface were in the range of 1.11 nm to 1.85 nm thick. The theoretical thickness existing in literature is 1.7 nm for a C_{12} alkane chain

Table 3-2 Thickness of SAMs Deposited on Gold-Coated Wafers, Pure and at Different Ratios.

Sample [(a)]	Pure $C_{12}H_{26}S$	Pure $SH(CH_2)_{11}OH$	1:1	1:2	2:1	4:1	1:4	5:1
Thickness (nm)	1.50	1.25	1.16	1.46	1.11	1.25	1.15	1.85
Std Deviation (n=3)	0.58	0.46	0.13	0.13	0.21	0.32	0.46	0.71

a) The ratios expressed in this table correspond to $C_{12}H_{26}S$: $SH(CH_2)_{11}OH$.

The concentrations of all solutions were 1mM. The gold-coated wafer treatment was done over night.

and 1.5 nm for a C_{11} [52] assuming a 20° to 30° tilt, an identical C-C bond, with a configuration in trans. Therefore, the acquired ellipsometric measurements showed reasonable results. These results indicated the presence of SAM onto the substrate surface before the PS-*b*-PMMA film deposition.

Characterization of PS-b-PMMA Films Deposited on SAM

PS-*b*-PMMA films were spin-cast onto gold-coated wafers that had received different treatments via SAM deposition. These substrates presented dissimilar water contact angle measurements, therefore had different surface energies. Figure 3-3 describes the relationship between θ^{water} and the PS-*b*-PMMA film thickness. The results showed that for θ^{water} ranging from 20° to 100°, the PS-*b*-PMMA film thickness did not vary significantly. The obtained data suggested that the thickness of PS-*b*-PMMA film was independent of the surface energy of the substrate.

PS-*b*-PMMA films were characterized using AFM. Figure 3-4 shows tapping mode AFM images of PS-*b*-PMMA films spin-casted onto a gold substrate, having different thicknesses (a) 22.1 nm thick, and (b) 41.4 nm thick after the annealing process. In Figure 3-4a, circular bumps were observed, suggesting that the PMMA domains were oriented perpendicular to the film surface [51]. In Figure 3-4b, lamellar structures were present, suggesting that the PMMA domains were oriented parallel to the film surface. The obtained data suggested that the PMMA domains orientation was related to the thickness of PS-*b*-PMMA films, as previously shown by Guarini et al. [53].

PS-*b*-PMMA films presenting the similar thicknesses of 41.5nm +/- 0.1nm were deposited onto gold-coated wafers possessing different θ^{water}. Figure 3-5 shows tapping mode AFM images of PS-*b*-PMMA films spin-casted onto gold substrates having extreme θ^{water} (a) 101°, and (b) 24.8° before the spin-casting process. In both Figure 3-5a and Figure 3-5b, lamellar structures were present, suggesting that the PMMA domains were oriented parallel to the film surface. The obtained data suggested that the orientation of the PMMA domains in the PS-*b*-PMMA films was independent of the surface energy of the substrate. (Similar experiments done with SAM coated Si wafers led to the same conclusions: see supplementary data in Appendix A)

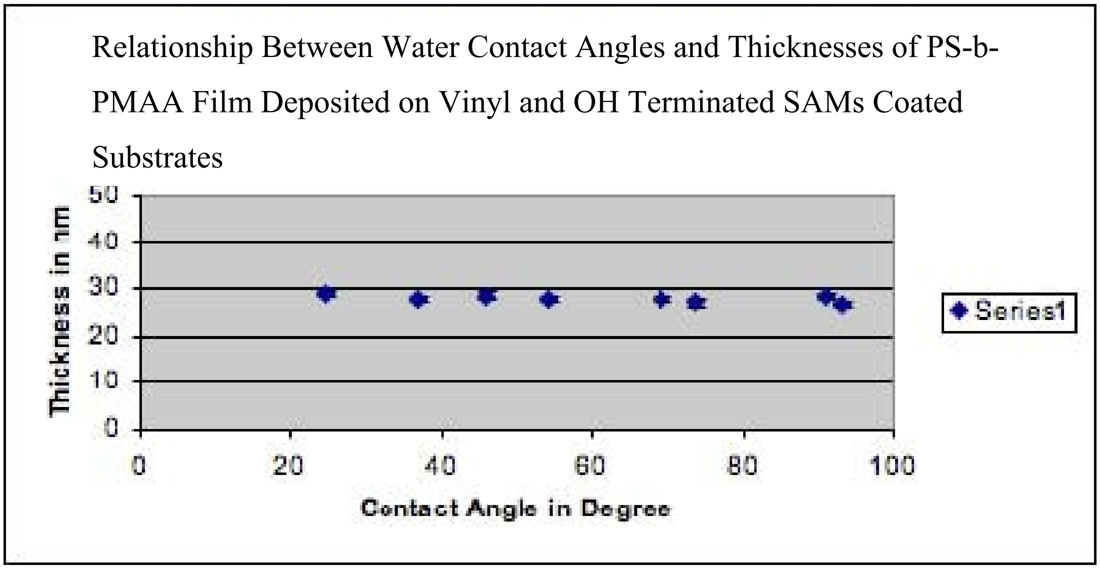

Figure 3-3 Graph showing the Relationship between θ^{water} and the Thickness of PS-*b*-PMMA Deposited on Vinyl and Hydroxy Terminated SAM Coated Substrates.

The concentrations of all solutions were 1mM. The gold-coated wafer treatment was done over night.

All standard deviations are ≤ 2nm, therefore they are barely visible on the graph.

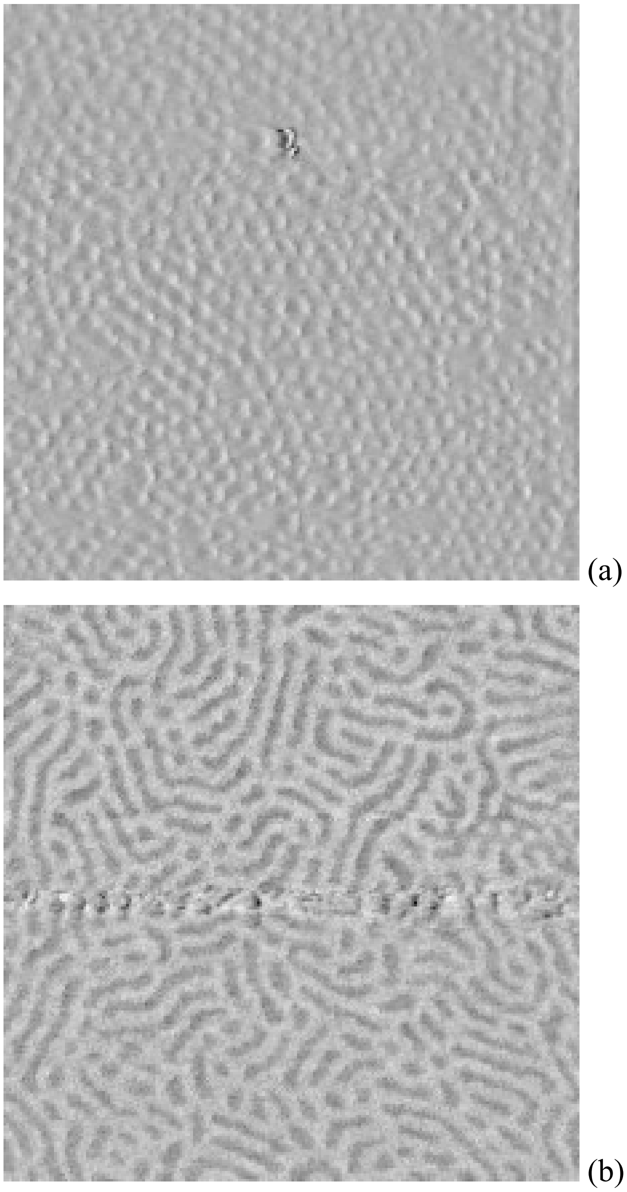

Figure 3-4 AFM Images of a 0.7% PS-*b*-MMA Films (a) Thickness = 22.1nm and (b) Thickness = 41.4 nm, Deposited on Vinyl Terminated SAM Treated Gold-Coated Wafer (1X1µm).

The concentrations of all solutions were 1mM. The gold-coated wafer treatment was done over night. Samples were annealed at 170°C under vacuum for 60h.

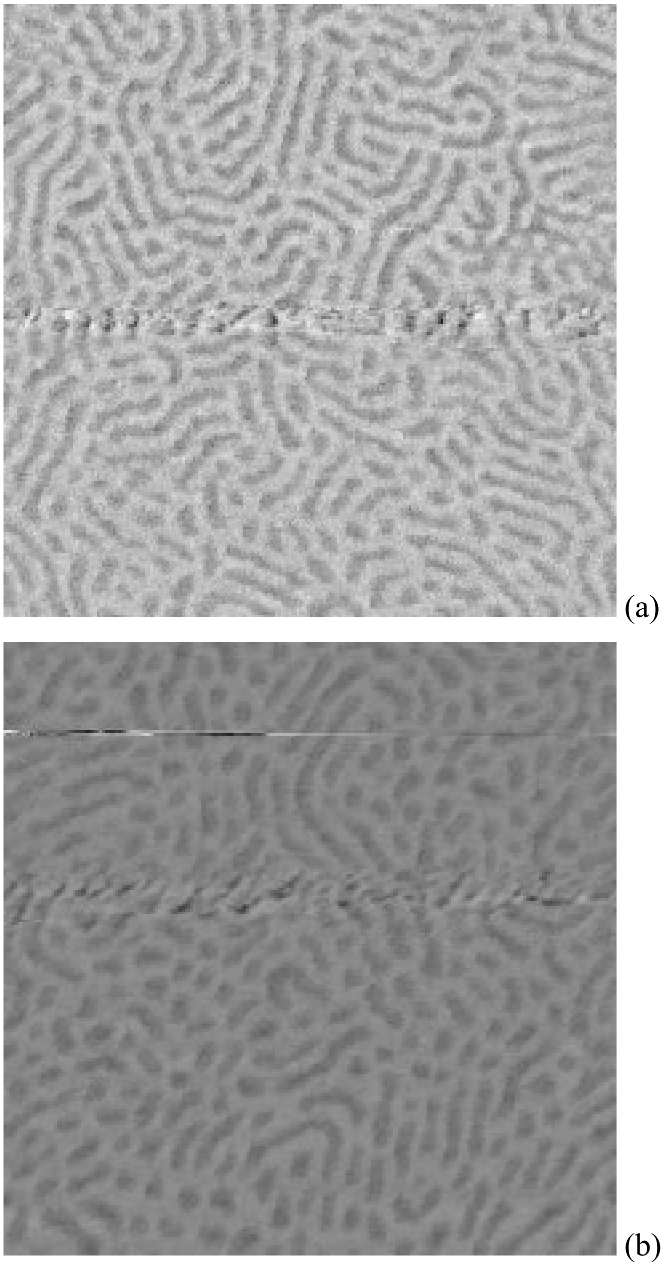

Figure 3-5 AFM Images (1X1µm) of 0.7% PS-*b*-MMA Films (t ~ 41.5nm) Deposited on (a) Vinyl Terminated SAM Treated Gold-Coated Wafer, and (b) Vinyl: OH (1:30) Terminated SAM Treated Gold-Coated Wafer.

The concentrations of all solutions were 1mM. The gold-coated wafer treatment was done over night.

Characterization of the SAM on Gold-Coated Wafer after Annealing Process

The obtained data implying that the orientation of the PMMA domains in the PS-*b*-PMMA films was independent of the surface energy of the substrate led us to think that the SAM might have been damaged during the annealing process. To verify if this was the case, and also at what temperature it would occur, the annealing procedure was conducted at different temperatures for gold-coated wafers treated with a variety of SAMs including pure carboxy, hydroxy, vinyl, and methyl terminated thiols, as well as some mixed together. Then, the θ^{water} was measured again and compared to the one obtained before annealing. The results are presented in Figure 3-6. This graph shows the stability of the SAM during the annealing process. It appeared that when the temperature of this procedure was increased, so did the θ^{water} of the hydroxy terminated thiol (yellow triangles). For the carboxy terminated (pink squares), methyl terminated (light blue crosses), and vinyl terminated (dark blue diamonds) thiols, their θ^{water} revealed to be relatively stable. To determine if they actually remained the same or if the SAMs were damaged whilst giving the same θ^{water} values, extra experiments were completed. These experiments allowed us to compare the θ^{water} of a surely damaged SAM (annealed in the presence of air) versus the θ^{water} described previously.

The effects of the change in atmosphere on the SAMs stability were also explored, and are presented in Figure 3-7. The annealing process was conducted at 120°C, both in vacuum and in air. Figure 3-7 clearly shows that the stability of SAM is greater when the annealing procedure is carried out in vacuum rather than in air. Furthermore, when the process is done in air, all the θ^{water} were aiming towards the same point which would be $75 < \theta^{water} < 95°$. This value would correspond to the one of a contaminated gold-coated wafer surface. Therefore, it is reasonable to assume that even though some SAMs were presenting a fairly stable θ^{water} at 170°C, they might actually have also been damaged during the annealing treatment.

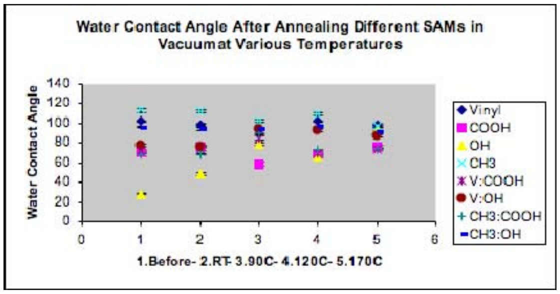

Figure 3-6 Graph Presenting the Stability of SAM when Exposed to Increasing Temperatures.

The concentrations of all solutions were 1mM. The gold-coated wafer treatment was done over night.

All standard deviations vary from 0.8 to1.8 degree, therefore they are barely visible on the graph.

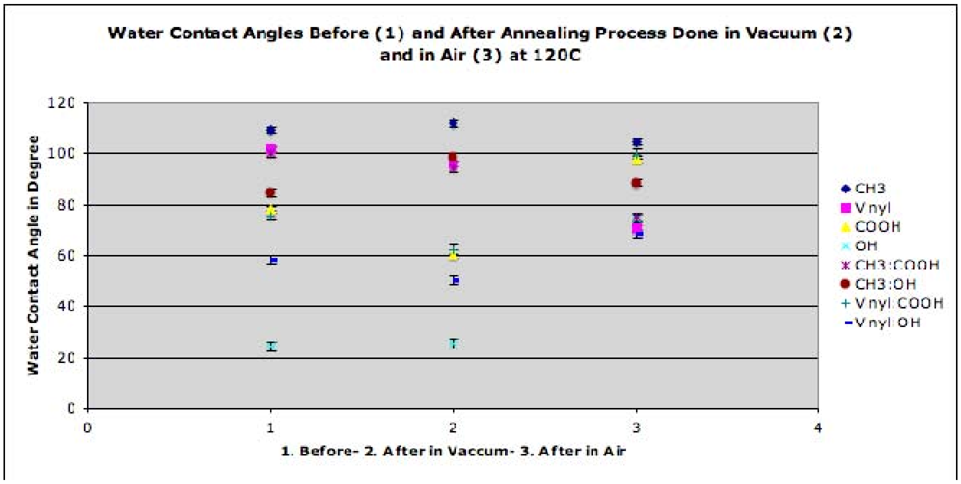

Figure 3-7 Graph Presenting the Effects of Vacuum vs. Air During the Annealing Process.

The concentrations of all solutions were 1mM. The gold-coated wafer treatment was done over night. The annealing process was conducted at 120°C.

All standard deviations vary from 1.0 to1.9 degree; therefore they are barely visible on the graph.

Conclusion

This research investigated the relationship between the domains orientation in the diblock copolymer films and the surface energy of the substrate depending on the type of SAM coating it. Therefore, organic mercaptans forming SAM onto gold were used to tailor the surface energy of the substrate in order to investigate their effect on the diblock copolymer rearrangement, hence the importance of the SAM stability. The surface energy of the substrate did not seem to have any effect on the diblock copolymer morphology. Furthermore, the data obtained showed that these SAMs were thermo sensitive and were damaged during the annealing process. If the surface energy could not account for the diblock copolymer rearrangement due to the thermo instability of SAMs, then what could? This question was investigated in Chapter 4.

References

1. Poirier, G. E.; Pylant, E. D. *Science* (*Washington D.C.*) **1996**, *272*, 1145.

2. Nuzzo, R. G.; Allara, D. L. *J. Am. Chem. Soc.* **1983**, *105*, 4481.

3. Porter, M. D.; Bright, T. D.; Allara, D. L.; Chidsey, C. E. D. *J. Am. Chem. Soc.* **1987**, *109*, 3449.

4. Dubois, L. H.; Nuzzo, R. G. *Annu. Rev. Phys. Chem.* **1992**, *43*, 437.

5. Bain, C. D.; Evall, J.; Whitesides, G. M. *J. Am. Chem. Soc.* **1989**, *111*, 7155.

6. Bain, C. D.; Whitesides, G. M. *Science (Washington, D.C.)* **1988**, *240*, 62.

7. Biebuyck, H. A.; Bain, C. D.; Whitesides, G. M. *Langmuir* **1994**, *10*, 1825.

8. Laibinis, P.E.; Whitesides, G. M.; Allara, D. L.; Tao, Y. T.; Parikh, A. N.; Nuzzo, R. G. *J. Am. Chem. Soc.* **1991**, *113*, 7152.

9. Dubois, L. H.; Zegarski, B. R.; Nuzzo, R. G. *J. Chem. Phys.* **1993**, *98*, 678.

10. Roy, D.; Fendler, J. J. *Adv. Mater***.** **2004**, *16*, 479.

11. Whitesides, G. M.; Laibinis, P. E. *Langmuir* **1990**, *6*, 87.

12. Bain, C. D.; Troughton, E. B.; Tao, Y. T.; Evall, J.; Whitesides, G. M.; Nuzzo, R. G. *J. Am. Chem. Soc.* **1989**, *111*, 321.

13. Dannenberger, O.; Wolff, J. J.; Buck, M. *Langmuir* **1998**, *14*, 4679.

14. Yamada, R.; Sakai, H.; Uosaki, K. *Chem. Lett.* **1999**, 667.

15. Ishida, T.; Mizutani, W.; Azehera, H.; Sato, F.; Choi, N.; Akiba, U.; Fujihara, M.; Tokumoto, H. *Langmuir* **2001**, *17*, 7459.

16. Kawasaki, M.; Sato, T.; Tanaka, T.; Takao, K. *Langmuir* **2000**, *16*, 1719.

17. Yamada, R.; Wano, H.; Uosaki, K. *Langmuir* **2000**, *16*, 5523.

18. Laibinis, P. E.; Fox, M. A.; Folkers, J. P.; Whitesides, G. M. *Langmuir* **1991**, *7*, 3167.

19. Lay, M. D.; Varazo, K.; Stickney, J. L. *Langmuir* **2003**, *19*, 8416.

20. O'Dwyer, C.; Gay, G.; de Lesegno, B. V.; Weiner, J. *Langmuir* **2004**, *20*, 8172.

21. Rai, B.; Sathish, P.; Malhotra, C. P.; Pradip, Ayappa, K. G. *Langmuir* **2004**, *20*, 3138.

22. Zhang, Z. S.; Wilson, O. M.; Efrenov, M. Y.; Olson, O. A.; Braun, P. V.; Senaratne, W.; Ober, C. K.; Zhang, M.; Allen, L. H. *Appl. Phys. Lett.* **2004**, *84,* 5198.

23. Brandini, P.; Stroeve, P. *Macromolecules* **2003**, *36*, 9492.

24. Brandini, P.; Stroeve, P. *Macromolecules* **2003**, *36*, 9502.

25. Kim, S. O.; Solak, H. H.; Stoykovich, M. P.; Ferrier, N. J.; De Pablo, J. J.; Nealey, P. F. *Nature* **2003**, *424*, 411.

26. Patai, S.; Rappoport, Z. *The Chemistry of Organic Derivatives of Gold and Silver* Wiley and Sons Ltd **1999.**

27. Alpha-SE Software Manual version 2.06 by J.A. Woollam Co, Inc.

28. Walsh, C. B.; Frances, E. I. *Science* **1999**, *347*, 167.

29. Dulcey, C. et al. *Langmuir* **1996**, *12,* 1638.

30. Jeong, U.; Ryu, D. Y.; Kim, J. K.; Kim, D. H.; Russell, T. P.; Hawker, C. J. *Adv. Mater.* **2003**, *15*, 1247.

31. Park, M.; Harrison, C.; Chaikin, P. M.; Register, R. A.; Adamson, D. H. *Science* **1997**, *276*, 1401.

32. Thurn-Albrecht, T. et al. *Science* **2000**, *290*, 2126.

33. Lopes, W. A.; Jaeger, H. M. *Nature* **2001***, 414*, 735.

34. Chan, V. Z. H. et al. *Science* **1999**, *286*, 1716.

35. Chang, J. Y.; Ross, C. A.; Thomas, E. L.; Smith, H. I.; Vansco, G. J. *Appl Phys. Lett.* **2002**, *81*, 3657.

36. Bodycomb, J.; Funaki, Y.; Kimishima, K.; Hashimoto, T. *Macromolecules* **1999**, *32*, 2075.

37. Rosa, C. D.; Park, C.; Thomas, E. L.; Latz, B. *Nature* **2000**, *405*, 433.

38. Mansky, P.; Liu, Y.; Huang, E.; Russell, T. P.; Hawker, C. *Science* **1997**, *275*, 1458.

39. Mao, H.; Hillmayer, M. A. *Macromolecules* **2005**, *38*, 4038.

40. Thurn-Albrecht, T.; Steiner, R.; DeRouchey, J.; Stafford, C. M.; Huang, E.; Bal, M.; Tuominen, M.; Hawker, C. J.; Russell, T. P. *Adv. Mater.* **2000**, *12*, 787

41. Huang, E.; Rockford, L.; Russell, T. P.; Hawker, C. J.; Mays, J. *Nature* **1998**, *395*, 757.

42. Russell T. P. et al. *Macromolecules* **1998**, *31*, 8509.

43. Russell T. P. et al. *Polymer* **2001**, *42*, 9091.

44. Ryu, D. Y.; Russell, T. P. *Science* **2005**, *308*, 236.

45. Jeong, U.; Russell, T. P. *Macromolecules* **2003**, *36*, 3626.

46. Thurn-Albrecht, T.; DeRouchey, J.; Russell, T. P.; Jaeger, H. M. *Macromolecules* **2000**, *33*, 3250.

47. Xu, T.; Goldbach, J. T.; Misner, M. J.; Kim, S.; Gibaud, A.; gang, O.; Ocko, B.; Guarini, K. W.; Black, C. T.; Hawker, C. J.; Russell, T. P. *Macromolecules* **2004**, *37*, 2972.

48. Thurn-Albrecht, T. et al. *Science* **2000**, *290*, 2126.

49. Misner, M. J.; Skaff, H.; Emrick, T.; Russell, T. P. *Adv. Mater.* **2003**, *15*, 221.

50. Xu, T.; Hawker, C. J.; Russell, T. P. *Macromolecules* **2005**, *38*, 2802.

51. Fasolka, M. J.; Mayes, A. M. *Annu. Re*V. *Mater. Res.* **2001**, *31*, 323.

52. "An Introduction to Ultrathin Organic Films from Langmuir-Blodgett to Self-Assembly" Ulman, A. **1991** Academic Pres, Inc.

53. Guarini, K. W.; Black, C. T.; Milkove, K. R.; Sandstrom, R. L. *J. Vac. Sci. Technol. B*, **2001**, *19*, 2784.

CHAPTER 4 - Diblock Copolymer Orientation via Substrate Roughness

Introduction

This chapter describes the roughness-induced orientation of cylindrical domains in thin films of polystyrene–poly(methylmethacrylate) diblock copolymer (PS-*b*-PMMA; 0.3 as the volume fraction of PMMA). Atomic force microscopy (AFM) and cyclic voltammetry (CV) were used to assess the orientation of cylindrical PMMA domains in PS-*b*-PMMA films having different thicknesses (20-200 nm) on various substrates having different surface roughness and hydrophilicity. AFM exhibited the orientation of PMMA domains at the free film surface. CV on gold substrates coated with PS-*b*-PMMA films whose PMMA domains were chemically removed permitted us to discuss the domain orientation at the polymer–substrate interface and also inside the film. If the PMMA domains reach the substrate surface, a current proportional to the electrode area exposed is observed.

In a BCP film supported by a substrate, the orientation of cylindrical domains is strongly affected by interactions at the BCP–substrate interface and at the free surface of the BCP film. Preferential wetting of one fragment at an interface leads to horizontal domain orientation. To align cylindrical domains vertically to an underlying substrate, the substrate surface has often been chemically tailored to balance the wettability of the BCP fragments.[12, 13] For example, such neutralized surfaces for PS-*b*-PMMA, where the surfaces have no preference for either PS or PMMA, were obtained on hydrogen-terminated Si,[14] on substrates modified with organosilane self-assembled monolayers,[15] and on substrates covalently modified with a brush layer of a PS-PMMA random copolymer having an appropriate volume fraction.[12, 16] In addition to controlling the surface wettability of the underlying substrates, several approaches have been simultaneously employed to improve the vertical alignment of cylindrical PMMA domains in a PS-*b*-PMMA film, including optimization of film thickness,[17, 18] addition of

PMMA homopolymers,[19] control of solvent-evaporation conditions,[20] and electric field application during annealing.[6, 11, 21]

Recently, Sivaniah and coworkers experimentally demonstrated that the roughness of a substrate surface induced the vertical alignment of lamellar PMMA domains in thin films of symmetric PS-*b*-PMMA.[22, 23] The domain orientation was influenced by the periodicity of the BCP domains, and the lateral periodicity and vertical amplitude of the surface corrugations of an underlying substrate. The roughness-induced vertical alignment of BCP domains was theoretically explained using a model based on the distortion of aligned domain structures by the rough surface.[24-26] The roughness-induced domain alignment provides a simple means for preparing PS-*b*-PMMA thin films containing vertically-aligned PMMA domains, because it does not require the chemical neutralization of the substrate surface.[22, 23]

In this chapter, the effects of substrate surface roughness and hydrophilicity on the orientation of cylindrical PMMA domains in thin films of asymmetric PS-*b*-PMMA instead of lamella-forming, symmetric PS-*b*-PMMA were investigated. AFM and CV were used to verify the orientation of cylindrical PMMA domains in PS-*b*-PMMA films having different thicknesses on different substrates.

Experimental

Chemicals

PS-*b*-PMMA (Average molecular weight of PS and PMMA: respectively 39,800 and 17,000; polydispersity: 1.06) was purchased from Polymer Source Inc., and used as received. Toluene (Fischer Chemical), hydrofluoric acid (Acros Organics), and ethanol were used without further purification. Solutions used for electrochemical measurements were prepared with water having a 18 MΩ cm or higher resistivity (Barnstead Nanopure System).

Substrates

Indium-tin-oxide (ITO) coated cover slips were prepared via sputtering of 100 nm ITO on glass cover slips (Metavac Transparent conductive coating 7163; 15 ohms/sq) and were purchased from Metavac (Holtsville, NY). Gold-coated silicon wafers (Au-Si) and were prepared via sputtering 10 nm Ti followed by 200 nm Au onto Si (100) wafer, were purchased from LGA Thin Films (Foster City, CA). Gold-coated glass slides (Au-glass) were prepared by electron-beam deposition of 100 nm Au onto aluminosilicate glass microscope slides with a thin Ti adhesion layer, and were purchased from Platypus Technologies (Madison, WI). Planar Si (100) wafers (p-type) were purchased from University Wafer (South Boston, MA).

Grain diameter was determined from cross section of AFM images. The measure was taken from bottom edges on both side of each grain, and average was calculated with n=30.

Cleaning of Substrates

All substrates were sonicated in ethanol for 10 minutes, dried with argon, and then cleaned in a Novascan PSD-UVT UV-Ozone system for 30 minutes. The surface hydrophobicity of a substrate, prior to the polymer film deposition, was assessed by measuring water contact angles (θ^{water}) reflecting the cleanliness of the surface. A water droplet (2 μL) was deposited onto a substrate surface, and the angles at the two opposite water-substrate interfaces were measured within 30 s after drop deposition.

*Preparation of PS-*b*-PMMA Films*

Thin PS-*b*-PMMA films were prepared from its toluene solution. PS-*b*-PMMA concentrations were varied to obtain different film thicknesses. PS-*b*-PMMA films were deposited on previously cleaned substrates via spin coating at 2000 rpm for 30 seconds. They were then annealed at 170ºC in vacuum (ca. 0.3 Torr) for 60 hours to allow the formation of the PMMA cylindrical domains in the films.

Techniques

AFM Measurements

AFM images were obtained by Tapping Mode imaging in air, using a Digital Instruments Multimode AFM with Nanoscope IIIa electronics. Probes for Tapping Mode AFM (cantilever length, 125 μm; force constant, 40 N/m; resonant frequency, 300 kHz) were purchased at Applied Nanostructures.

*PS-*b*-PMMA Films Thickness Measurements*

The thickness of PS-*b*-PMMA films was measured using a J. A. Woollam alpha-SE spectroscopic ellipsometer.

Electrochemical Measurements

CV measurements were performed in a three-electrode cell using a CH Instruments model 618B electrochemical analyzer, as reported previously.[28] The values and errors reported here are the averages and 90% confidence limits, respectively, obtained from multiple measurements on multiple samples.

Results and Discussion

Surface Roughness and Hydrophilicity of Planar Substrates

In this study, five types of planar substrates having different surface roughnesses and hydrophilicities were used as supports of PS-*b*-PMMA films: Si wafers treated in an aqueous HF solution (HF-Si), Si wafers treated in the UV-O_3 cleaner (O_3-Si), Au substrates prepared on Si wafer via sputtering (Au/Si), Au substrates prepared on aluminosilicate glass via electron-beam deposition (Au/glass), and ITO-coated glass coverslips (ITO). Figure 4-1 (left row) shows Tapping-mode AFM images of the substrate surfaces. Nanoscale grains were observed on the Au/Si, Au/glass and ITO surfaces. The HF-Si and O_3-Si surfaces were much smoother than the other substrates. Table 4-1 summarizes the root-mean-square (RMS) vertical displacement (R), grain diameter (d_g), and water contact angle (Θ^{water}) of these substrates. The surface roughness and grain diameter were larger in the order of ITO ≥ Au/glass > Au/Si > HF-Si ~ O_3-Si and Au/glass > ITO > Au/Si ≥ HF-Si ~ O_3-Si, respectively. The surfaces of O_3-Si and ITO were very hydrophilic ($\Theta^{\text{water}} \sim 10°$),[29, 30] the Au substrates were moderately hydrophilic ($\Theta^{\text{water}} \sim 30–45°$), and HF-Si was most hydrophobic ($\Theta^{\text{water}} \sim 75°$).

AFM Images of PS-b-PMMA Films Deposited on Smooth Si Substrates

Since the PMMA volume fraction of the PS-*b*-PMMA employed here was 0.3, annealed PS-*b*-PMMA films contain self-assembled cylindrical domains of the minor PMMA fragments. The right three rows in Figure 4-1 show Tapping-mode AFM images

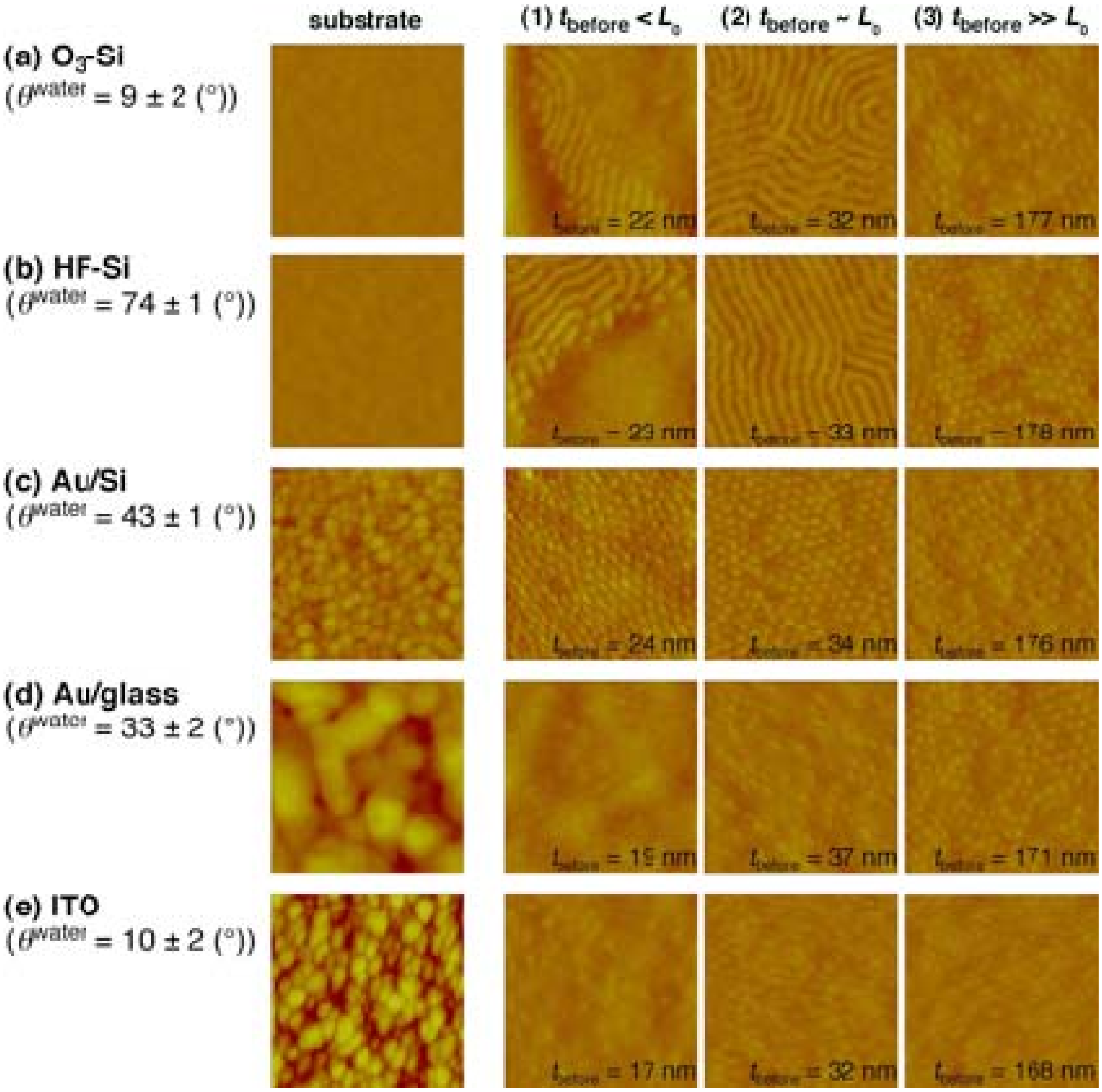

Figure 4-1 AFM images (500 x 500 nm^2)

(Left row) AFM images (500 x 500 nm^2; Δz = 40 nm) of the cleaned surfaces of (a) O_3-Si, (b) HF-Si, (c) Au/Si, (d) Au/glass and (e) ITO. (Right three rows) AFM images (500 x 500 nm^2; Δz = 20 nm)) of PS-*b*-PMMA film surfaces having different thicknesses (t_{before}) on (a) O_3-Si, (b) HF-Si, (c) Au/Si, (d) Au/glass and (e) ITO: (1) $t_{before} < L_0$; (2) $t_{before} \sim L_0$; (3) $t_{before} >> L_0$. The ellipsometric thickness of each film was included in each image. Image d-1 taken by Dr Takashi Ito. Image e-1 taken by Shaida Ibrahim.

of PS-*b*-PMMA thin films having different thicknesses on the five different substrates. The ellipsometric thickness (t_{before}) of the PS-*b*-PMMA films was (1) slightly smaller than the domain periodicity (L_0)[1] ($t_{\text{before}} < L_0$), (2) similar to L_0 ($t_{\text{before}} \sim L_0$), and (3) larger than L_0 ($t_{\text{before}} >> L_0$). The L_0 value and radius of PMMA domains (a) determined from these AFM images were 35 nm and 10 nm, respectively. These images clearly show that the surface features of PS-*b*-PMMA films were strongly affected by film thickness and underlying substrate.

Figure 4-1a shows AFM images of PS-*b*-PMMA films on O_3-Si. Their surface features were different according to the thickness of the polymer film. At $t_{\text{before}} \leq L_0$, PMMA domains were horizontally oriented to the free surface (Figure 4-1a-1 and 4-1a-2), reflecting the higher affinity of the PMMA fragments to the underlying O_3-Si surface[1] due to hydrogen bond interactions between surface Si-OH groups and the ester moieties of PMMA.[31] The horizontal domains formed island structures in PS-*b*-PMMA films at $t_{\text{before}} < L_0$ (Figure 4-1a-1) and covered the whole surface at $t_{\text{before}} \sim L_0$ (Figure 4-1a-2).[1, 8] These observations are consistent with the commensurability effects.[1, 12] In contrast, at $t_{\text{before}} >> L_0$ (Figure 4-1a-3), circular dots indicating cylindrical PMMA domains oriented vertically to the film surface were observed. The vertical domain orientation at the free surface probably originated from almost balanced affinity of the two polymer fragments to vacuum, rather than from the interactions at the polymer–substrate interface. The slightly smaller density of the domains (ca. 700 dots/μm^2) than the maximum density of the hexagonal domains calculated from the L_0 (ca. 900 dots/μm^2) may reflect the slightly higher affinity of PS to vacuum because of its lower surface tension.[32]

HF-Si surface was more hydrophobic than O_3-Si surface as shown by their Θ^{water} values (Table 4-1) because of the removal of the hydrophilic surface oxide layer by the HF treatment.[29] It was reported that a HF-treated Si served as a neutralized surface for PS and PMMA, having no preference for either PS or PMMA, gave vertically oriented cylindrical PMMA domains in thin PS-*b*-PMMA films.[14] However, in spite of the large difference in Θ^{water}, our AFM images of PS-*b*-PMMA films on HF-Si (Figure 4-1b) were similar to those on O_3-Si (Figure 4-1a). This result suggests that the HF-Si surface used in this study might be partially covered with the surface oxide that was preferentially wetted by the PMMA fragments. Indeed, the Θ^{water} value of our HF-Si was slightly smaller (~ 74°) than those reported for hydrogen-passivated Si surfaces (~ 80°).[29] The HF-Si surface was partially oxidized maybe during washing and drying the substrates. The similarity in AFM images of PS-*b*-PMMA films on the Si substrates having largely different hydrophilicities suggests that, for PS-*b*-PMMA films of $t_{\mathrm{before}} \le L_0$, the cylindrical PMMA domains were horizontally oriented on the smooth surface having Θ^{water} smaller than 75°.

AFM Images of PS-b-PMMA Films Deposited on Rougher Au and ITO Substrates

In contrast, the rougher Au and ITO substrates gave different trends in domain orientation. Figure 4-1c-e shows AFM images of PS-*b*-PMMA films on (c) Au/Si, (d) Au/glass and (e) ITO. At $t_{\mathrm{before}} >> L_0$ (Figure 4-1c-3, 4-1d-3 and 4-1e-3), a number of cylindrical PMMA domains were oriented vertically to the film surface, as with those on the Si surfaces (Figure 4-1a-3 and 4-1b-3). The density of the vertical domains exposed to the surface was similar for all the five images. These results supported our hypothesis that the domain orientation at the free surface of the thicker films was mainly determined by the interactions at the polymer–vacuum interface (*vide supra*).

In contrast, AFM images of PS-*b*-PMMA films at $t_{\mathrm{before}} < L_0$ and $t_{\mathrm{before}} \sim L_0$ were different according to the substrates. On Au/Si, vertical domains without any island structures were observed at $t_{\mathrm{before}} < L_0$ and $t_{\mathrm{before}} \sim L_0$ (Figure 4-1c-1, 4-1c-2). These AFM images suggest that the cylindrical PMMA domains on Au/Si were oriented vertically to the polymer–substrate and polymer–vacuum interfaces. Although it is not clear whether the Au/Si surface was preferentially wetted by the PS or PMMA fragments, the difference in the wettability of PS and PMMA to the surface should not be so large that the surface roughness could prevent the horizontal orientation of the cylindrical domains.[22]

On Au/glass, the AFM image at $t_{\mathrm{before}} < L_0$ (Figure 4-1d-1) reflected the surface morphology of the substrate. The PMMA domains were not clearly observed, perhaps because a layer parallel to the surface was formed on the large grains due to the preferential wetting of the PMMA fragments to the substrate ($\Theta^{\mathrm{water}} \sim 33°$; Table 4-1). At

$t_{\text{before}} \sim L_0$, the circular dots corresponding to vertical PMMA domains were observed (Figure 4-1d-2) although their density was smaller than that on Si/Au. The vertical domains in Figure 4-1d-2 seemed to be present at the edge of the grains as seen on AFM images, suggesting that the roughness prevented the horizontal orientation of the cylindrical domains.

AFM images of PS-*b*-PMMA films on ITO were similar to those on Au/glass with slightly larger density of the vertical domains at $t_{\text{before}} \sim L_0$ (Figure 4-1e-2 vs. 4-1d-2). The density of the vertical PMMA domains at $t_{\text{before}} \sim L_0$ was higher in the order of Au/Si (Figure 4-1c-2) > ITO (Figure 4-1e-2) > Au/glass (Figure 4-1d-2), which was opposite to the order of the grain size (Au/glass > ITO > Au/Si, Table 4-1). This trend may suggest that cylindrical domains in PS-*b*-PMMA films of $t_{\text{before}} \leq L_0$ can be efficiently aligned vertically to the surface when grain size on a substrate is close to L_0 of the BCP. More systematic investigations are required to reach this conclusion since this study only covered substrates having grains similar to or larger than L_0. Note that the ITO surface was very hydrophilic ($\Theta^{\text{water}} \sim 10°$; Table 4-1), which was comparable to that of O_3-Si. As with Si-OH groups on O_3-Si, -OH groups on ITO surface[33] would offer preferential wetting of ITO surface with PMMA rather than PS due to hydrogen bond interactions with the carbonyl groups of PMMA. However, the ITO gave vertically oriented cylindrical domains at $t_{\text{before}} \sim L_0$ (Figure 4-1e-2) in contrast to the O_3-Si that gave the horizontal domain orientation (Figure 4-1a-2). These results strongly suggest that the vertical domain orientation on the ITO was induced by the surface roughness of the substrate (Figure 4-4).

The above results suggest that the vertical orientation of the cylindrical domains could be obtained on surface having optimum roughness: grain diameter close to L_0 and moderate vertical deviations. This trend is different from the previous theoretical predictions[25, 26] and experimental results[22, 23] for lamellar domains in symmetric PS-*b*-PMMA films: For symmetric PS-*b*-PMMA, the vertical orientation was enhanced for rougher surfaces having larger corrugation amplitude and lateral periodicity.

Table 4-1 Surface Root-Mean-Squares Roughness (*R*), Grain Diameter on the Surface (d_g) and Water Contact Angle (θ^{water}) of the Substrate Surfaces Used in this Study.

Substrate	*R* (nm) [a)]	d_g (nm)[b)]	θ^{water} (°) [c)]
O_3-Si	0.2 ± 0.0	–[d)]	9 ± 2
HF-Si	0.3 ± 0.1	–[d)]	74 ± 1
Au/Si	1.4 ± 0.2	36 ± 5	43 ± 1
Au/glass	3.1 ± 0.4	132 ± 13	33 ± 2
ITO	3.5 ± 0.8	54 ± 6	10 ± 2

[a)] Average and 90% confidence limit of the root-mean-square (RMS) vertical displacement of at least three separate samples. [b)] The average and 90% confidence limit of the diameters of surface grains obtained from line profiles of AFM images. [c)] Average and 90% confidence limit, determined from at least three separate samples. [d)] The surfaces were too smooth to recognize the grains in the line profiles of AFM images.

Comparison of CVs on Au/Si and Au/glass Coated with PS-b-PMMA-Derived Nanoporous Films

A redox current measured using electrochemical methods reflects the diffusion of redox species onto the electrode in addition to the kinetics of the electron transfer reaction between the redox species and electrode.[34] Thus, electrochemical methods have been used to characterize the geometry and surface properties of nanopores.[28, 35-38]

For example, using CV, Dr Ito and his group previously assessed the removal of the PMMA domains from thin (ca. 30 nm thick) PS-*b*-PMMA films on Au/Si, and identified the surface functional groups on PS-*b*-PMMA-derived nanopores.[28] Here, CVs of 1,1'-ferrocenedimethanol ($Fc(CH_2OH)_2$) were measured on Au/Si and Au/glass coated with PS-*b*-PMMA-derived nanoporous films having different thicknesses. The nanoporous films were obtained by etching PMMA domains in PS-*b*-PMMA films via UV irradiation and subsequent sonication in AcOH. The domain orientation in the original (unetched) PS-*b*-PMMA films could be deduced from CV data that would reflect the nanoporous structure of the etched PS-*b*-PMMA films. Uncharged $Fc(CH_2OH)_2$ was used to assess the permeability of the film through the nanopores with no influence of the nanopore surface charge.[28]

Figure 4-2a shows CVs of $Fc(CH_2OH)_2$ on Au/Si and Au/glass coated with PS-*b*-PMMA-derived nanoporous films of $t_{\mathrm{before}} \sim L_0$. The PMMA domains were etched to form cylindrical nanopores that would expose the underlying gold surface, allowing $Fc(CH_2OH)_2$ in the aqueous solution for diffusing to the electrode surface.[28] Figure 4-3 summarizes the relationship between the maximum current and t_{before}, obtained from multiple separate samples. The maximum current on Au/Si substrates coated with the nanoporous films of t_{before} = 28~40 nm was 50 ± 4 μA, which was similar to the peak current calculated using parameters obtained from the AFM images (the pore density: 900 pores/μm^2; pore radius: 10 nm), as reported previously.[28] This coincidence may suggest that most of the nanopores in the films, i.e., the PMMA domains in the original PS-*b*-PMMA films, on Au/Si reached the underlying gold surface.[28] Figure 4-2a also shows that Au/glass gave a slightly smaller redox current than Au/Si. Similar trends were obtained for nanoporous films having t_{before} between 30 nm and 100 nm (Figure 4-

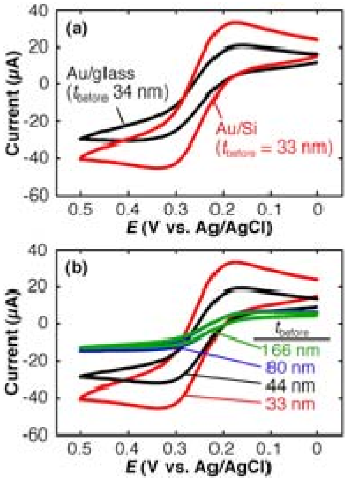

Figure 4-2 CVs (scan rate 0.05 V/s) of 3.0 mM $Fc(CH_2OH)_2$ in 0.1 M KNO_3 on Different Substrates

(a) CVs (scan rate 0.05 V/s) of 3.0 mM $Fc(CH_2OH)_2$ in 0.1 M KNO_3 on Au/Si and Au/glass coated with PS-*b*-PMMA films ($t_{before} \sim L_0$) after the removal of the PMMA domains. (b) CVs (scan rate 0.05 V/s) of 3.0 mM $Fc(CH_2OH)_2$ in 0.1 M KNO_3 on Au/Si coated with PS-*b*-PMMA films having different t_{before} after the removal of the PMMA domains. Data taken by Dr. Yongxin Li.

3). The smaller current on the Au/glass would be ascribed to the smaller density of vertical PMMA domains at the polymer–substrate interface, as suggested by the AFM images (Figure 4-1d-2).

CVs of Au/Si Coated with PS-b-PMMA-Derived Nanoporous Films Having Different Thicknesses

Figure 4-2b shows CVs of $Fc(CH_2OH)_2$ for PS-*b*-PMMA-derived nanoporous films having different thicknesses on Au/Si. With increasing the film thickness, peak-shaped CVs were changed to sigmoidal CVs, reflecting the transition from the linear to radial diffusion modes.[34, 39] In addition, the maximum current decreased upon increasing the film thickness from 30 to 80 nm, and then reached a plateau (Figure 4-3). The transition from peak-shaped to sigmoidal CVs with increasing the film thickness probably reflected a decrease in the density of recessed nanoelectrodes exposed by the PMMA etching. The decrease in the nanoelectrode density increased the spacing between neighboring nanoelectrodes, and thus provided isolated radial diffusion layers from individual nanoelectrodes to give the sigmoidal CVs. Assuming the uniform distribution of the isolated recessed nanoelectrodes on the substrate, the density of open nanopores can be calculated using the following equation:[39, 40]

$$i_{\mathrm{lim}} = \frac{4\pi nFCDa^2N}{4t + \pi a} \qquad (1)$$

In this equation, n is the number of electrons ($n = 1$ for $Fc(CH_2OH)_2$), F is Faraday's constant (= 96485 C/mol), D is the diffusion coefficient of $Fc(CH_2OH)_2$ (= 6.4 x 10^{-6} cm^2/s),[41] C (mol/cm^3) is its concentration (= 3.0 x 10^{-6} mol/cm^3), a is pore radius (~ 10 nm), and t is the pore length (~ film thickness). N, the number of the active nanoelectrodes, can be described as follows:[39]

$$N = \pi r^2 d \qquad (2)$$

where r is the radius of the O-ring that defines the area in contact with the solution (= 0.33 cm), and d is the density of the active nanoelectrodes. For PS-*b*-PMMA-derived nanoporous films of t_{before} ~170 nm on Au/Si, the average limiting currents were 21.3 µA (Figure 4-3), giving d = 6.0 pores/μm^2. Although the effective interelectrode

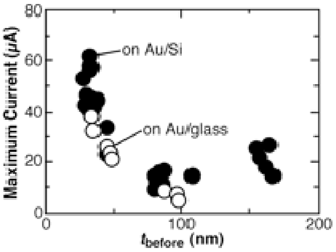

Figure 4-3 Maximum Anodic Current of $Fc(CH_2OH)_2$ in CVs (scan rate 0.05 V/s) on Au/Si (filled circles) and Au/glass (open circles) Coated with PS-*b*-PMMA Films having Different t_{befor} after the Removal of the PMMA Domains.

Data taken by Dr. Yongxin Li.

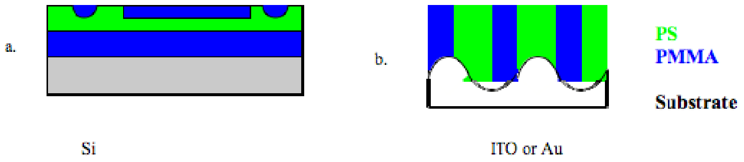

Figure 4-4 Scheme Representing the Orientation of PS-*b*-PMMA Domains in Thin Films on Flat (Si) and Rough (Au/Si, ITO) Substrates.

spacing (= 440 nm), calculated from the *d*, was smaller than the thickness of the diffusion layer (~ 26 μm at 0.05 V/s as scan rate),[34, 39] the observation of the sigmoidal CVs would be possible since the interelectrode spacing was >10 times larger than the pore diameter.[42] More importantly, this density value is much smaller than the density of vertical PMMA domains at the free surface (ca. 700 pores/μm^2; Figure 4-1c-3), suggesting that most of the PMMA domains exposed to the surface did not reach the underlying electrode to involve the electrode reaction. This is a big contrast to a nanoporous film of $t_{\mathrm{before}} \sim L_0$ on Au/Si, which gave peak-shaped CVs whose peak currents were similar to that estimated from the pore density obtained from the corresponding AFM images (*vide supra*).[28]

Orientation of Cylindrical PMMA Domains in PS-b-PMMA Films Immobilized on Au/Si Estimated from the AFM and CV Data

Based on the AFM and CV data, we can estimate the orientation of cylindrical PMMA domains in PS-*b*-PMMA films having different thicknesses on Au/Si (Figure 4-5). AFM images of PS-*b*-PMMA films on Au/Si (Figures 4-1c) showed cylindrical PMMA domains oriented vertically at the free surface over the thickness range of 20-200 nm. This observation seemingly suggested that the PMMA domains penetrated vertically from the free surface to the substrate interface regardless of the film thickness (Figure 4-5).

However, the CV data suggested that the density of the nanoelectrodes formed by the PMMA removal depended on the film thickness. At $t_{\mathrm{before}} \leq L_0$, the density of the nanoelectrodes was close to that of the surface-exposed vertical PMMA domains, suggesting that most of the PMMA domains were aligned vertically from the free surface to the underlying substrate (Figure 4-5a). At this thickness range, the domain orientation throughout the film was primarily determined by the interactions between the polymer and the substrate, and the roughness of the substrate induced the vertical orientation of the cylindrical PMMA domains.

At $t_{\mathrm{before}} > L_0$, cylindrical PMMA domains were aligned vertically to the free surface, but most of them did not reach the underlying electrode, as suggested by the

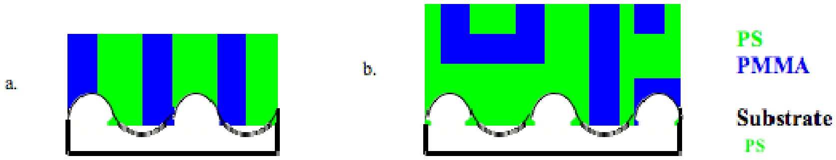

Figure 4-5 Scheme Representing the Orientation of PS-*b*-PMMA Domains in Films having Different Thicknesses on Au/Si Substrate.

sigmoidal CVs (Figure 4-2b) and the electrode density from the limiting current (*vide supra*). These results suggest that the domains would change the orientation within the film (Figure 4-5b), as previously observed using cross-sectional transmission electron microscopy (TEM).[13] In these thicker films, the domain orientation would be determined by the interactions at the polymer–vacuum interface in addition to those at the polymer–substrate interface. This disorganized domain orientation within the film may result from involvement of the different domain alignment mechanisms at the two interfaces.

Conclusion

This chapter has described the effects of substrate properties and film thickness on the orientation of cylindrical PMMA domains in thin films of PS-*b*-PMMA. Since AFM and CV gave complementary information on the polymer films, these techniques would provide simple means for investigating the domain structure in PS-*b*-PMMA films, as compared to cross-sectional TEM,[17, 22, 23] dynamic secondary ion mass spectroscopy[13, 23] and neutron reflectivity measurements.[12, 13] In PS-*b*-PMMA films of thickness close to its L_0, the vertical domain orientation could be obtained on substrates having an optimal surface roughness without neutralizing the affinity of the PS and PMMA fragments. In contrast, in a thicker film, the roughness-induced orientation was not sufficient to vertically align cylindrical domains from the underlying substrate to the free surface. Thus, other approaches such as electric field application[6, 11, 21] would be required to obtain a high-density array of vertically-oriented cylindrical domains. The roughness-induced domain orientation on unneutralized surface was reported for lamella-forming PS-*b*-PMMA films,[22, 23] and was explained theoretically.[25, 26] However, the effects of the substrate roughness on the domain orientation in cylinder-forming PS-*b*-PMMA did not completely follow the theory for the roughness-induced orientation of lamella domains.[25, 26] Thus, more experimental and also theoretical research would be necessary to fully understand the orientation of cylindrical domains in cylinder-forming PS-*b*-PMMA films on rough surfaces.

References

(1) Fasolka, M. J.; Mayes, A. M. *Annu. Rev. Mater. Res.* **2001**, *31*, 323-355.

(2) Li, M.; Coenjarts, C. A.; Ober, C. K. *Adv. Polym. Sci.* **2005**, *190*, 183-226.

(3) Hillmyer, M. A. *Adv. Polym. Sci.* **2005**, *190*, 137-181.

(4) Olson, D. A.; Chen, L.; Hillmyer, M. A. *Chem. Mater.* **2008**, *20*, 869-890.

(5) Park, M.; Harrison, C.; Chaikin, P. M.; Register, R. A.; Adamson, D. H. *Science* **1997**, *276*, 1401-1404.

(6) Thurn-Albrecht, T.; Schotter, J.; Kastle, G. A.; Emley, N.; Shibauchi, T.; Krusin-Elbaum, L.; Guarini, K.; Black, C. T.; Tuominen, M. T.; Russell, T. P. *Science* **2000**, *290*, 2126-2129.

(7) Kim, H.-C.; Jia, X.; Stafford, C. M.; Kim, D. H.; McCarthy, T. J.; Tuominen, M.; Hawker, C. J.; Russell, T. P. *Adv. Mater.* **2001**, *13*, 795-797.

(8) Darling, S. B.; Yufa, N. A.; Cisse, A. L.; Bader, S. D.; Sibener, S. J. *Adv. Mater.* **2005**, *17*, 2446-2450.

(9) Zhang, Q.; Xu, T.; Butterfield, D.; Misner, M. J.; Ryu, D. Y.; Emrick, T.; Russell, T. P. *Nano Lett.* **2005**, *5*, 357-361.

(10) Yang, S. Y.; Ryu, I.; Kim, H. Y.; Kim, J. K.; Jang, S. K.; Russell, T. P. *Adv. Mater.* **2006**, *18*, 709-712.

(11) Thurn-Albrecht, T.; Steiner, R.; DeRouchey, J.; Stafford, C. M.; Huang, E.; Bal, M.; Tuominen, M.; Hawker, C. J.; Russell, T. P. *Adv. Mater.* **2000**, *12*, 787-791.

(12) Mansky, P.; Russell, T. P.; Hawker, C. J.; Pitsikalis, M.; Mays, J. *Macromolecules* **1997**, *30*, 6810-6813.

(13) Huang, E.; Russell, T. P.; Harrison, C.; Chaikin, P. M.; Register, R. A.; Hawker, C. J.; Mays, J. *Macromolecules* **1998**, *31*, 7641-7650.

(14) Xu, T.; Kim, H.-C.; DeRouchey, J.; Seney, C.; Levesque, C.; Martin, P.; Stafford, C. M.; Russell, T. P. *Polymer* **2001**, *42*, 9091-9095.

(15) Niemz, A.; Bandyopadhyay, K.; Tan, E.; Cha, K.; Baker, S. M. *Langmuir* **2006**, *22*, 11092-11096.

(16) Mansky, P.; Liu, Y.; Huang, E.; Russell, T. P.; Hawker, C. *Science* **1997**, *275*, 1458-1460.

(17) Fasolka, M. J.; Banerjee, P.; Mayes, A. M.; Pickett, G.; Balazs, A. C. *Macromolecules* **2000**, *33*, 5702-5712.

(18) Guarini, K. W.; Black, C. T.; Milkove, K. R.; Sandstrom, R. L. *J. Vac. Sci. Technol. B* **2001**, *19*, 2784-2788.

(19) Jeong, U.; Ryu, D. Y.; Kho, D. H.; Kim, J. K.; Goldbach, J. T.; Kim, D. H.; Russell, T. P. *Adv. Mater.* **2004**, *16*, 533-536.

(20) Xuan, Y.; Peng, J.; Cui, L.; Wang, H.; Li, B.; Han, Y. *Macromolecules* **2004**, *37*, 7301-7307.

(21) Thurn-Albrecht, T.; DeRouchey, J.; Russell, T. P.; Jaeger, H. M. *Macromolecules* **2000**, *33*, 3250-3253.

(22) Sivaniah, E.; Hayashi, Y.; Iino, M.; Hashimoto, T.; Fukunaga, K. *Macromolecules* **2003**, *36*, 5894-5896.

(23) Sivaniah, E.; Hayashi, Y.; Matsubara, S.; Kiyono, S.; Hashimoto, T.; Fukunaga, K.; Kramer, E. J.; Mates, T. *Macromolecules* **2005**, *38*, 1837-1849.

(24) Podariu, I.; Chakrabarti, A. *J. Chem. Phys.* **2000**, *113*, 6423-6428.

(25) Tsori, Y.; Andelman, D. *Macromolecules* **2003**, *36*, 8560-8566.

(26) Tsori, Y.; Sivaniah, E.; Andelman, D.; Hashimoto, T. *Macromolecules* **2005**, *38*, 7193-7196.

(27) Jeong, U.; Ryu, D. Y.; Kim, J. K.; Kim, D. H.; Russell, T. P.; Hawker, C. J. *Adv. Mater.* **2003**, *15*, 1247-1250.

(28) Li, Y.; Maire, H. C.; Ito, T. *Langmuir* **2007**, 12771-12776.

(29) Williams, R.; Goodman, A. M. *Appl. Phys. Lett.* **1974**, *25*, 531-532.

(30) Koh, S.; McDonald, K. D.; Holt, D. H.; Dulcey, C. S.; Chaney, J. A.; Pehrsson, P. E. *Langmuir* **2006**, *22*, 6249-6255.

(31) Ulman, A. *Chem. Rev.* **1996**, *96*, 1533-1554.

(32) Gong, Y.; Joo, W.; Kim, Y.; Kim, J. K. *Chem. Mater.* **2008**, *20*, 1203-1205.

(33) Purvis, K. L.; Lu, G.; Schwartz, J.; Bernasek, S. L. *J. Am. Chem. Soc.* **2000**, *122*, 1808-1809.

(34) Bard, A. J.; Faulkner, L. R. *Electrochemical Methods, Fundamentals and Applications, 2nd Ed.*; Wiley: New York, 2001.

(35) Zhang, B.; Zhang, Y.; White, H. S. *Anal. Chem.* **2004**, *76*, 6229-6238.

(36) Wang, G.; Zhang, B.; Wayment, J. R.; Harris, J. M.; White, H. S. *J. Am. Chem. Soc.* **2006**, *128*, 7679-7686.

(37) Jeoung, E.; Galow, T. H.; Schotter, J.; Bal, M.; Ursache, A.; Tuominen, M. T.; Stafford, C. M.; Russell, T. P.; Rotello, V. M. *Langmuir* **2001**, *17*, 6396-6398.

(38) Laforgue, A.; Bazuin, C. G.; Prud'homme, R. E. *Macromolecules* **2006**, *39*, 6473-6482.

(39) Ito, T.; Audi, A. A.; Dible, G. P. *Anal. Chem.* **2006**, *78*, 7048-7053.

(40) Bond, A. M.; Luscombe, D.; Oldham, K. B.; Zoski, C. G. *J. Electroanal. Chem.* **1988**, *249*, 1-14.

(41) Fan, F.-R. F. *J. Phys. Chem. B* **1998**, *102*, 9777-9782.

(42) Bartlett, P. N.; Taylor, S. L. *J. Electroanal. Chem.* **1998**, *453*, 49-60.

CHAPTER 5 - Assessing Nanopores Formation via AFM and CV[5]

Introduction

This chapter describes electrochemical characterization of nanoporous films prepared from PS-*b*-PMMA immobilized on Au-Si substrate. CV was used to assess the completeness of chemical etching of the cylindrical PMMA domains from an annealed PS-*b*-PMMA film. The annealing process has been extensively used to damage PMMA through UV exposure and subsequent acidic treatment. AFM only gives an external view of the BCP films, exposing pores left after PMMA removal. However, this technique does not indicate the extent of that removal, nor does it prove that the pores actually go through the whole film and reach the bottom surface. It will also account for the domains orientation within the film. The challenge was to find a way to show that the extent of the PMMA orientation and its removal without damaging the films.

The use of a ratio 7:3 for PS: PMMA BCP ensures the cylindrical formation of PMMA as shown in Figure 1-1. However, it does not affect the orientation of those domains within the PS matrix. It is then crucial to use a non-invasive yet reliable technique to confirm the PMMA domains are orthogonal to the substrate surface. As the substrate is Au-Si wafer, an electrochemical technique seems to be suited; it will not damage the sample, and it is very dependable.

Equations 2-4 and 2-5 show the direct relationship between current and electrode area. Therefore, it is possible to calculate the expected electrode area exposed by using AFM images, assuming that all the pores seen on the surface of the film are totally open and reach the electrode surface. Then, the current obtained through CV measurement will confirm the actual exposed area of the Au-Si substrate. Therefore, the extent of the PMMA removal will be determined, as well as the perpendicular orientation of the pores.

In contrast to AFM and Fourier transform infrared-external reflection spectroscopy (FTIR-ERS), CV could detect the extent of exposure of the bottom gold surface in a non-destructive manner and prove that a recessed nanodisk-array electrode (RNE) structure was made.

Experimental

Chemicals

Glacial acetic acid (Fisher Scientific) was used as received. Potassium nitrate (Fischer Chemical), 1,1'-ferrocenedimethanol ($Fc(CH_2OH_2)_2$; Aldrich Chemical) were of reagent grade quality or better and used without further purification. Solutions prepared for electrochemical measurements purposes were based on water having an 18 MΩ cm or higher resistivity (Barnstead Nanopure System).

Methods

PMMA domains were degraded by UV irradiation for 80 minutes using the Novascan PSD-UVT UV-Ozone system under argon atmosphere at λ=250nm, after a 20 minutes argon purge of the chamber. During the UV exposure, the PS domains cross-linked forming a solid matrix while the PMMA was deteriorated as it was broken at the ester bond. However, the films were not damaged. A following sonication in glacial acetic acid disposed of the PMMA debris to expose the open nanopores. Then, the samples were thoroughly rinsed with water.

Techniques

AFM Measurements

AFM images were obtained by Tapping Mode imaging in air, using a Digital Instruments Multimode AFM with Nanoscope IIIa electronics. Probes for Tapping Mode AFM (cantilever length, 125 μm; force constant, 40 N/m; resonant frequency, 300 kHz) were purchased at Applied Nanostructures.

Spectroscopic Ellipsometer Measurements

A J. A. Woollam alpha-SE spectroscopic ellipsometer was used to determine if the films suffered any damage during the PMMA removal process.

Fourier Transform Infrared External Reflection Spectroscopy (FTIR-ERS)

FTIR-ERS measurements of thin PS-*b*-PMMA films were performed in dry air using a Nicolet Protege 460 spectrophotometer equipped with a Harrick Seagull reflection accessory (Pleasantville, NY) and a TGS detector. All spectra were the sum of 256 scans obtained at 2 cm^{-1} resolution using p-polarized light at an 80° angle of incidence with respect to the gold substrate. Spectra of the PS-*b*-PMMA-coated gold substrates were obtained by subtracting the spectrum of a cleaned gold substrate.

Electrochemical Measurements

CV measurements were performed in a three-electrode cell containing a Ag/AgCl (3 M KCl) reference electrode and a Pt counter electrode using a CH Instruments model 618B electrochemical analyzer. A polymer coated gold substrate (serving as the working electrode) was immobilized at the bottom of the cell. The diameter of the film area in contact with the solution, which was defined by a circular hole formed on the upper glass plate, was 0.65 cm. The pH of the solution was adjusted by adding a dilute solution of KOH or HCl and supporting electrolyte.

Results and Discussion

Characterization of PS-b-PMMA Films before and after Removal of the PMMA Domains Using AFM and FTIR-ERS

Prior to electrochemical measurements, PS-*b*-PMMA films on gold substrates were characterized using AFM and FTIRERS methods. Figure 5-1 shows tapping-mode AFM images of a PS-*b*-PMMA film (ca. 20 nm thick) on a gold substrate (a) before and (b) after PMMA etching.[1, 2] In Figure 5-1a, circular bumps having radius of 10.6 (1.5 nm were observed, suggesting that the PMMA domains were oriented perpendicular to the film surface.[3] After UV irradiation (10 min, 20 mW/cm2, λ=250nm) and subsequent AcOH treatment, the circular bumps changed to circular depressions with 10.5 +/- 1.4nm radius due to the removal of the PMMA domains (Figure 5-1b). Very similar AFM images were obtained for PS-*b*-PMMA films in the thickness range of 20-30 nm. As shown in Figure 5-1, AFM could be used to observe the removal of PMMA domains from a PS-*b*-PMMA film surface. However, it is not possible to discuss whether the PMMA domains were removed completely from the film so that the resulting nanopores reached the bottom gold surface. The removal of the PMMA domains could also be observed using FTIR-ERS. Figure 5-2 shows FTIR-ERS spectra of PS-*b*-PMMA films obtained before and after UV-AcOH treatment. The spectrum of a PS-*b*-PMMA film prior to UV-AcOH treatment (Figure 5-2a) exhibits absorption bands characteristics of PMMA and PS, including 1731 cm^{-1} (C=O of the ester groups in PMMA), 1188 and 1145 cm^{-1} (C-O stretching of the ester groups in PMMA), and 3023 cm^{-1} (-CH- stretching from benzene rings in PS). Upon increasing the UV irradiation time, the intensities of the bands assigned to PMMA decreased, whereas those of PS did not change significantly (Figure 5-2b-d). UV irradiation for 15 min degraded most of the PMMA segments in the film, and thus the PMMA domains could be removed by subsequent acetic acid treatment. However, the peak at 1731 cm-1 was found in FTIR-ERS spectra of the PS-*b*-PMMA films even after UV irradiation for 15 min (Figure 5-2d). This peak is ascribed to the

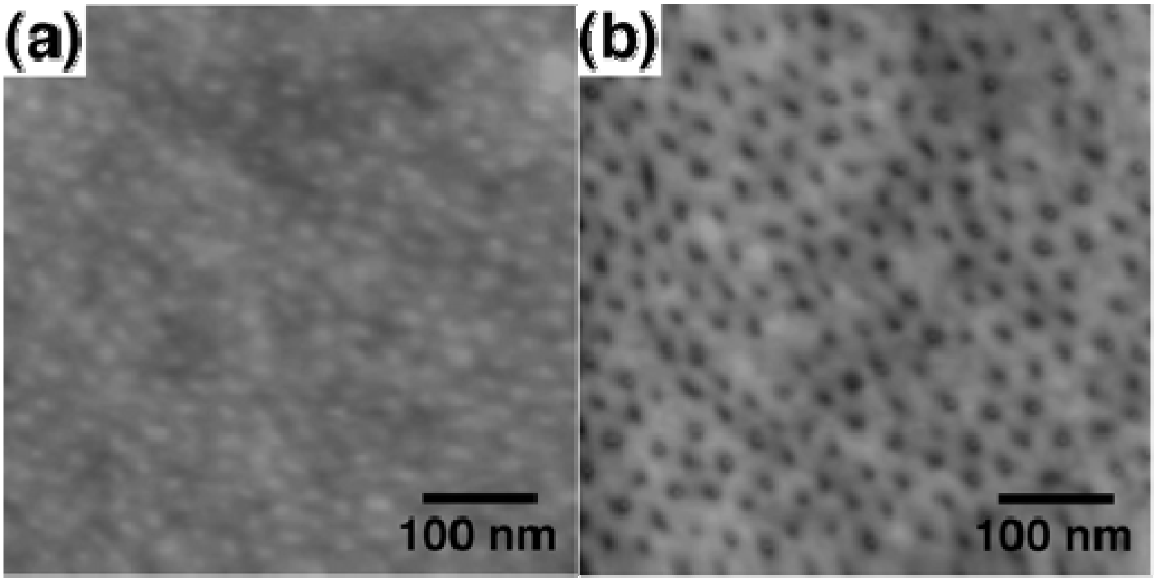

Figure 5-1 Tapping-Mode AFM Images of the Surfaces of a Thin PS-*b*-PMMA Film (ca. 20 nm Thick) on a Gold Substrate.[5]

(a) After the annealing at 170 C in vacuum (ca. 0.3 Torr) for 60 h and (b) after the removal of the PMMA domains via UV irradiation (10 min) and subsequent acetic acid treatment.

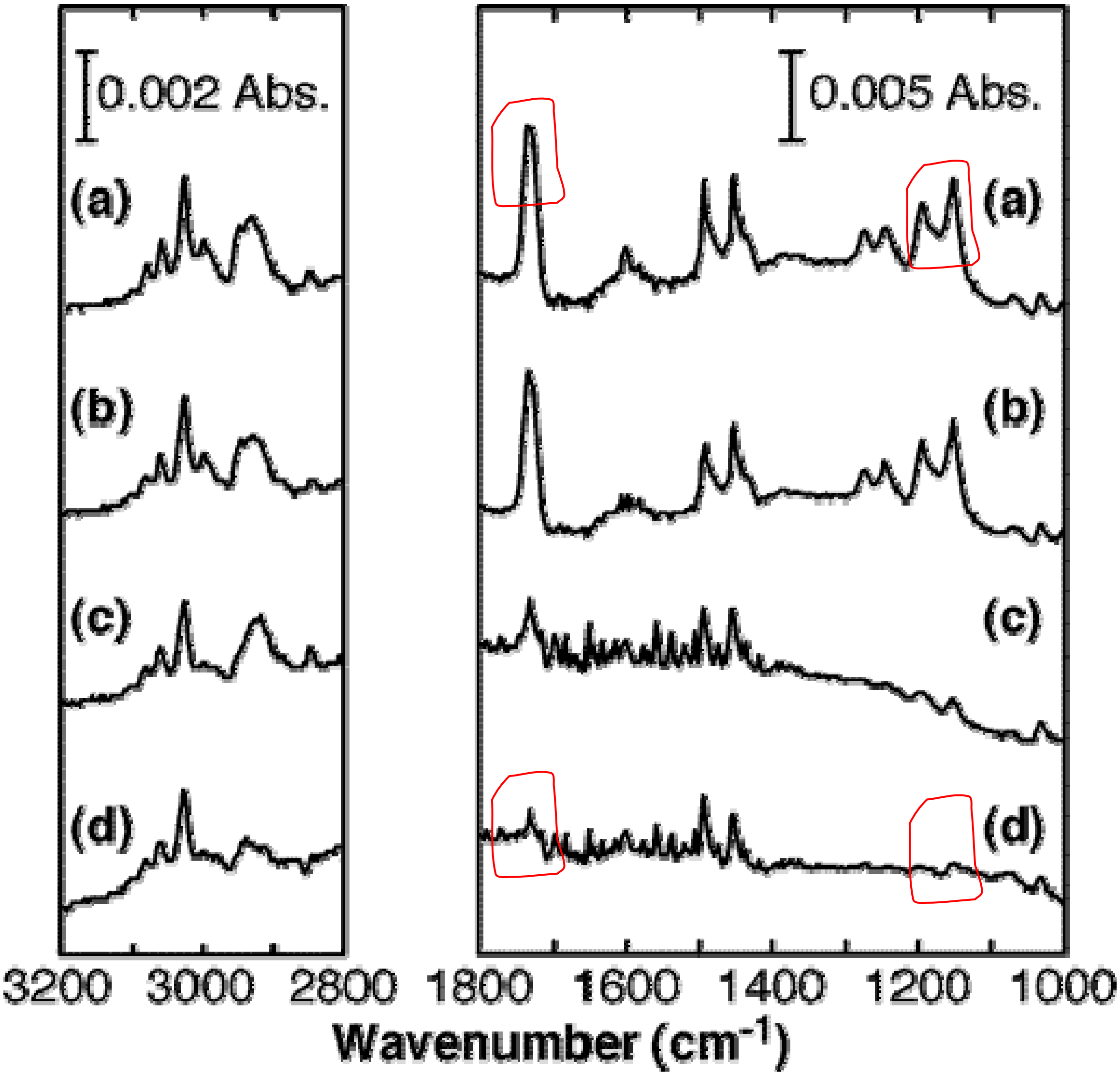

Figure 5-2 FTIR External Reflection Spectra of PS-*b*-PMMA Thin Films (ca. 30 nm thick) on Gold Substrates.[5]

(a) Before UV irradiation and after UV radiation for (b) 5 min, (c) 10 min, and (d) 15 min. The samples were treated in acetic acid (AcOH) for 2 min after being irradiated by UV light.

The intensity of the absorption bands characteristic of PMMA: 1731 cm^{-1} (C=O of the ester groups in PMMA), 1188 and 1145 cm^{-1} (C-O stretching of the ester groups in PMMA), decreases when UV irradiation time increases. Data taken by Dr. Yongxin Li.

ester carbonyl groups of residual PMMA units linked with the PS domains. Peaks due to other carbonyl groups (e.g., 1760 cm^{-1} for monomeric -COOH, and 1710 cm^{-1} for dimers) [4] were not observed in these spectra. The peak intensity of the ester carbonyl band in Figure 5-2d suggests that the vast majority of the PMMA (>90%) was degraded and removed from the film by UV irradiation for 15 min and subsequent acetic acid treatment. These results indicate that FTIR spectra can be used to assess the extent of the removal of the PMMA domains in a PS-*b*-PMMA film. However, FTIR spectra cannot be used to assess the exposure of the gold surface at the bottom of the nanoporous film.

Electrochemical Characterization of the Removal of the PMMA Domains in a PS-b-PMMA Film

Both AFM and FTIR-ERS provided conclusive evidence for the removal of the PMMA domains from PS-*b*-PMMA films. However, it was not possible to discuss whether the resulting cylindrical nanopores formed in the process reached the gold surface to form the RNE structure (Figure 5-3b). In contrast, electrochemical methods provide a simple means for characterizing the RNE structure, as discussed below. In this study, the PS-*b*-PMMA films were deposited directly on cleaned gold substrates without a buffer layer used to balance the affinities of PS and PMMA. If the gold surface is preferentially wetted by the PS, the nanopores formed will not reach the bottom gold, because PS will form an insulating layer that cannot be removed via UV-AcOH treatment (Figure 5-3a).[3] The presence of the insulating layer will affect the redox current in CV, because the layer will inhibit the electrode reaction of redox species in solution. On the other hand, if the PMMA wets the gold surface, the resulting nanoporous film cannot be stably immobilized on the gold surface (Figure 5-3).[3] In this case, the redox current will be similar to that on a bare gold electrode because of the detachment of the nanoporous film from the electrode surface. Figure 5-4a shows CVs of 3.0 mM $Fc(CH_2OH)_2$ in 0.1 M KNO_3 on gold substrates coated with PS-*b*-PMMA films (ca. 30 nm thick) after UV irradiation for the specified time (t_{UV}). The redox currents of $Fc(CH_2OH)_2$ increased for longer irradiation times. UV irradiation for 2 min did not give a peak-shaped CV because of the polymer layer remaining on the gold surface, which inhibited the electrode reaction

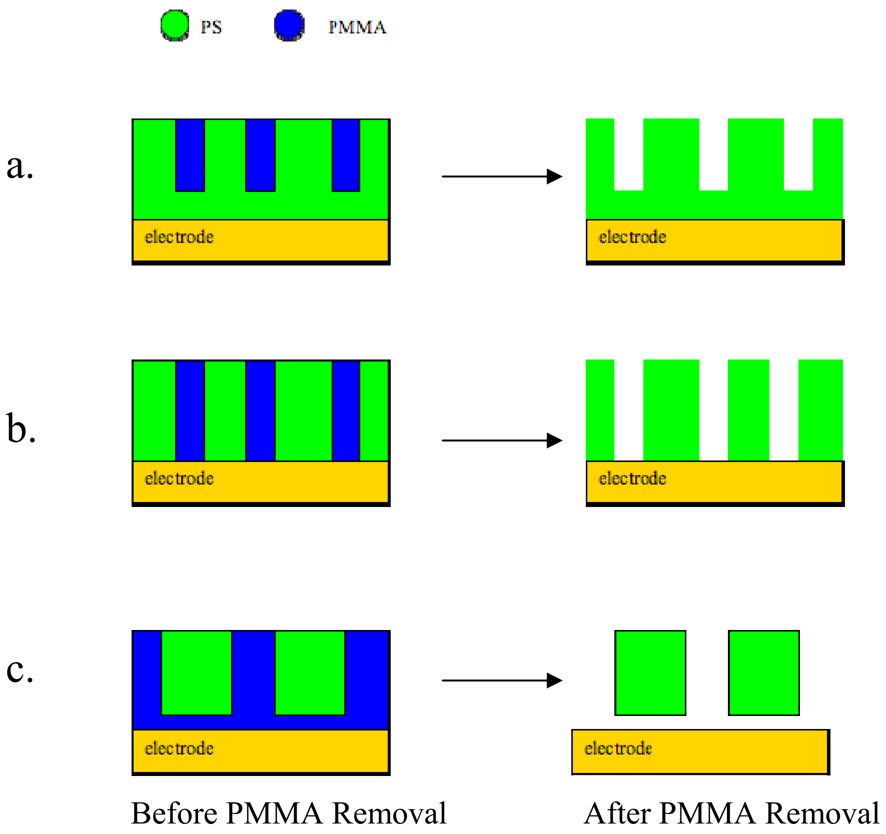

Figure 5-3 Assessment of the Removal of PMMA Domains.

of $Fc(CH_2OH)_2$. CVs for t_{UV} 10 min are quasi reversible (the potential difference between oxidation and reduction peaks (ΔE_p) is ~100 mV) with similar peak current (i_p) for the oxidation of $Fc(CH_2OH)_2$, suggesting that the PMMA domains were almost completely removed from the PS-*b*-PMMA films to form a RNE structure. As shown in Figure 5-4b, the i_p value reached a plateau for films irradiated for 10-15 min. The i_p values at the plateau were smaller than that on bare gold electrodes, which is indicated by the grey solid line in Figure 5-4b).

If the PMMA domains are completely removed to form the RNE structure (Figure 5-5b), i_p will be determined by the cross-sectional area defined by the nanopores. The AFM image shown in Figure 5-1b gives the pore radius (a = 10.5 nm) and density (~900 pores/μm^2). The pore density corresponds to 36 nm as the average spacing between adjacent nanopores, assuming that the nanopores are packed in a hexagonal arrangement. The pore spacing is much smaller than the thickness of the diffusion layer on the time scale of the CV measurements (e.g., ~20 μm thick for CV at 0.1 V/s scan rate). [6-8] Diffusion layers developed from individual nanopores will thus overlap on the time scale of the CV measurements, resulting in peak-shaped CVs.[8-10] In addition, since the thickness of the film, i.e., pore length, was very small (~30 nm) as compared with the thickness of the diffusion layer, the CVs obtained were very similar to those obtained with nanodisk electrode arrays with no recession.[6, 11]

According to theory, [11] the peak current expected from overlapped diffusion layers should be similar to that calculated from the geometrical area with no insulating layer, which was supported by previous reports.[12] In contrast, we reproducibly observed peak-shaped CVs with smaller peak currents even after the PMMA domains were likely removed completely (Figure 5-4)

There are a number of papers that have reported peak-shaped CVs with smaller peak currents for nanoporous anodic alumina membranes[7] and self-assembled monolayers[13, 14] in the presence of overlapped diffusion layers. Interestingly, the peak currents in the plateau region shown in Figure 5-4 were similar to that (49 μA) estimated using eq 1[6] from the total area of the gold disk electrodes exposed by the nanopores

$$I_p = 0.466nFAC\,(nFD\upsilon/RT)^{1/2} \qquad (1)$$

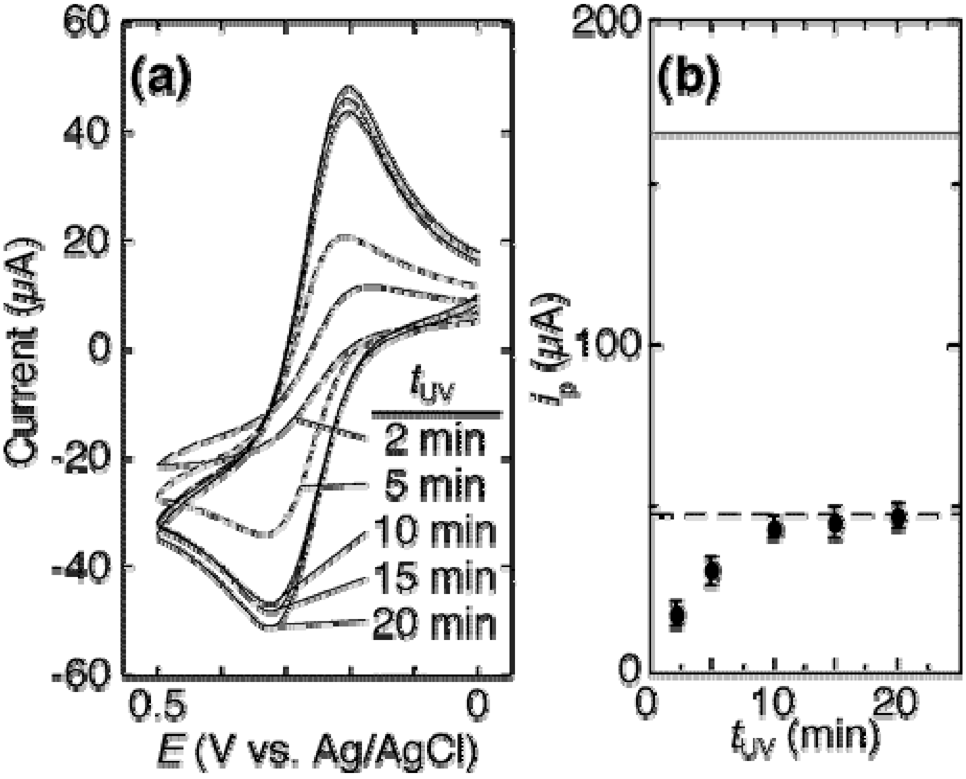

Figure 5-4 a) CVs (scan rate 0.05 V/s) of 3.0 mM $Fc(CH_2OH)_2$ in 0.1 M KNO_3 on Gold Electrodes Coated with Thin PS-*b*-PMMA Film (ca. 30 nm Thick) at Different UV Irradiation Times (b) Relationship between UV Irradiation Time and anodic Peak Current in CVs of 3 mM $Fc(CH_2OH)_2$. [5]

The plots and error bars indicate the averages and standard deviations obtained from at least three separate electrodes. The average peak current obtained on bare gold electrodes (grey solid line) and theoretical peak current calculated from the average pore diameter (21 nm) and pore density (900 pores/m^2) obtained from Figure 5-1 (dashed line) are also shown. Data taken by Dr Yongxin Li.

where n is the number of electrons ($n = 1$ for the redox-active molecules used in this study), F is Faraday's constant (96485 C/mol), R is the gas constant (8.31 J/K mol), T is temperature (298 K), A is the electrode area [$N\pi a^2$; a is the average radius of nanopores; N is the number of exposed nanopores, and can be calculated from the density of the pores (900 pores/μm^2) and electrode area defined by the circular hole in the glass cell (0.65 cm in diameter)], D is the diffusion coefficient of the redox-active species [7.6×10^{-6} cm^2/s for $Fe(CN)_6^{3-}$ and 6.4×10^{-6} cm^2/s for $Fc(CH_2OH)_2$],[6,16] and C (mol/cm^3) is its concentration. As expected from eq 1, a linear relationship was obtained on our nanoporous electrodes between i_p and $v^{1/2}$ for both redox molecules at $v < 0.1$ V/s. Furthermore, the slope of the line obtained is similar to that estimated from the active electrode area, diffusion coefficient, and concentration of the redox species in each case. This agreement suggests that, at $t_{UV} \geq 10$ min, the PMMA domains of the PS-*b*-PMMA film were almost completely degraded and removed to expose the bottom gold surface, which is consistent with the FTIR results discussed above (Figure 5-2). The polymer layer remaining on the gold electrode at the bottom of the nanopores after the PMMA degradation (see Figure 5-3a) would be negligible, as suggested by the very small influence of pH on the reversibility of the CVs (vide infra). In addition, the reproducible and repeatable observation of the CVs shown in Figure 5-4 indicates that the nanoporous film strongly adhered to the gold surface without the detachment of the nanoporous film from the gold substrate (see Figure 5-3c). The vertical orientation of the PMMA domains in the original PS-*b*-PMMA film on the bare gold was probably obtained due to roughness-induced orientation, [15] considering the gold surface contains grains having average diameters of ca. 30 nm and a root-mean squares roughness of ca. 2 nm (data not shown). These results indicate that CV can be used to assess the exposure of the bottom electrode as a result of the chemical etching processes of the PMMA domains and also to confirm the vertical orientation of the etchable domains.

Conclusion

In this chapter, electrochemical characterization of nanoporous films prepared from PS-*b*-PMMA immobilized on a Au-Si substrate was obtained via quantitative analysis of the CV data which provided a quick and simple means for monitoring the completeness of the chemical etching of the cylindrical PMMA domains from a thin PS-*b*-PMMA film while preserving the sample intact, as well as confirming the actual orientation of the pores.

References

1. Thurn-Albrecht, T. et al. *Science* **2000**, *290*, 2126.
2. Thurn-Albrecht, T.; Steiner, R.; DeRouchey, J.; Stafford, C. M.; Huang, E.; Bal, M.; Tuominen, M.; Hawker, C. J.; Russell, T. P. *Adv. Mater.* **2000**, *12*, 787.
3. Fasolka, M. J.; Mayes, A. M. *Annu. Rev. Mater. Res.* **2001**, *31*, 323.
4. Nakanishi, K.; Solomon, H. *Infrared Absorption Spectroscopy*; Holden-Day: San Francisco, CA, 1977.
5. Li, Y.; Maire, H. C.; Ito, T. *Langmuir* **2007**, *23*, 12771.
6. Bard, A. J.; Faulkner, L. R. *Electrochemical Methods, Fundamentals and Applications,* 2nd ed.; Wiley: New York, 2001; pp 619-623.
7. Brumlik, C. J.; Martin, C. R.; Tokuda, K. *Anal. Chem.* **1992**, *64*, 1201.
8. Ito, T.; Audi, A. A.; Dible, G. P. *Anal. Chem.* **2006**, *78*, 7048.
9. Arrigan, D. W. M. *Analyst* **2004**, *129*, 1157.
10. Zoski, C. G.; Yang, N.; He, P.; Berdondini, L.; Koudelka-Hep, M. *Anal. Chem.* **2007**, *79*, 1474.
11. Amatore, C.; Saveant, J. M.; Tessier, D. *J. Electroanal. Chem.* **1983**, *147*, 3.
12. Cheng, I. F.; Whiteley, L. D.; Martin, C. R. *Anal. Chem.* **1989**, *61*, 762.
13. Chailapakul, O.; Crooks, R. M. *Langmuir* **1993**, *9*, 884.
14. Grancharov, G.; Khosravi, E.; Wood, D.; Turton, A.; Kataky, R. *Analyst* **2005**, *130*, 1351.
15. Sivaniah, E.; Hayashi, Y.; Matsubara, S.; Kiyono, S.; Hashimoto, T.; Fukunaga, K.; Kramer, E. J.; Mates, T. *Macromolecules* **2005**, *38*, 1837.
16. Fan, F.-R. F. *J. Phys. Chem. B* **1998**, *102*, 9777.

CHAPTER 6 - Conclusions and Future Direction

In this dissertation, the effects of substrate surface roughness and hydrophilicity on the orientation of cylindrical PMMA domains in thin films of asymmetric PS-*b*-PMMA were investigated. Treatment of the substrate with self-assembled-monolayers (SAM), led to various surface hydrophilicities, but experiments to try to determine the orientation of the PMMA domains in the PS matrix were inconclusive. The effects of substrate properties and film thickness on the orientation of cylindrical PMMA domains in thin films of PS-*b*-PMMA were described. Since AFM and CV gave complementary information on the polymer films, these techniques provided simple means for investigating the domain structure in PS-*b*-PMMA films. In PS-*b*-PMMA films of thickness close to its L_0, the vertical domain orientation could be obtained on substrate having an optimal surface roughness without neutralizing the affinity of the PS and PMMA fragments. In contrast, in a thicker film, the roughness-induced orientation was not sufficient to vertically align cylindrical domains from the underlying substrate to the free surface. Thus, other approaches such as electric field application[1-3] would be required to obtain a high-density array of vertically-oriented cylindrical domains.

This study has demonstrated that CV measurements can be used to assess the chemical etching of the cylindrical PMMA domains in a PS-*b*-PMMA film while preserving the sample intact, as well as confirming the actual orientation of the pores. It can also be employed to measure the effective pore radius in the nanoporous polymer film. [5]

As a future direction, this electrochemical technique could be used to assess the presence of certain chemical groups within the pore walls of this type of sample made with PS-*b*-PMMA. CV measurements have the ability to recognize the presence of -COOH groups on the nanopore surface, leading to pH dependent changes in the surface charge of the nanopores. The surface functional groups cannot be detected using other characterization techniques conventionally used for the BCP based nanopores. On the basis of the findings reported [5], Ito's group is exploring the covalent modification of the surface-COOH groups via amidation to control the surface chemistry of the BCP-based nanopores. These results will be reported elsewhere. Covalent modification to control the surface chemistry within BCP-based nanopores and electrochemical characterization of the nanopore surfaces will make it possible to optimize BCP-based nanoporous materials for a variety of applications. In addition, the pH-based control of the effective nanopore radius shown by Dr. Li X. et al.[5] will provide a means for size-selective deposition of nanoparticles into BCP-based nanopores via electrophoresis. [4]

Also, more experiments can be done concerning the orientation of the cylindrical domains by using different types of substrates. Rougher or grainier surfaces could be utilized in order to observe how the PMMA domains would position themselves within the PS matrix. For instance, a sputter coater could be used to spread a thin gold film on top of a glass substrate. The number of gold coatings can be varied to obtain various roughnesses and grain sizes.

References

1. Thurn-Albrecht, T.; Schotter, J.; Kastle, G. A.; Emley, N.; Shibauchi, T.; Krusin-Elbaum, L.; Guarini, K.; Black, C. T.; Tuominen, M. T.; Russell, T. P. *Science* **2000**, *290*, 2126.
2. Thurn-Albrecht, T.; Steiner, R.; DeRouchey, J.; Stafford, C. M.; Huang, E.; Bal, M.; Tuominen, M.; Hawker, C. J.; Russell, T. P. *Adv. Mater.* **2000**, *12*, 787.
3. Thurn-Albrecht, T.; DeRouchey, J.; Russell, T. P.; Jaeger, H. M. *Macromolecules* **2000**, *33*, 3250.
4. Zhang, Q.; Xu, T.; Butterfield, D.; Misner, M. J.; Ryu, D. Y.; Emrick, T.; Russell, T. P. *Nano Lett.* **2005**, *5*, 357
5. Li, Y.; Maire, H. C.; Ito, T. *Langmuir* **2007**, *23*, 12771.

Appendix A - Tapping Mode AFM Images (1X1μm) of Annealed PS-*b*-PMMA Thin Films

Table A-1 On Different Types of Substrates: a) Ozone Exposed, b) Amine Terminated SAM Coated, c) Alkyl Terminated SAM Coated, d) HF Treated, and e) Gold Coated, Set #1.

Film Thickness Before Annealing in nm (yellow), θ^{water} in degree (red).

Substrate	**Si-O$_2$ $^{(a)}$**	**Si-N term $^{(b)}$**	**Si-CH$_3$ term $^{(c)}$**	**Si-HF $^{(d)}$**	**Au-Si $^{(e)}$**
[PS-*b*-PMMA] 0.50% wt	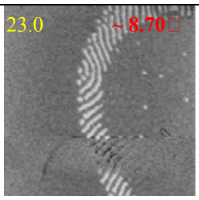 *611a05a*	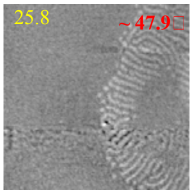 *628a05b*	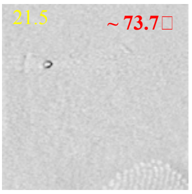 *822a05a*	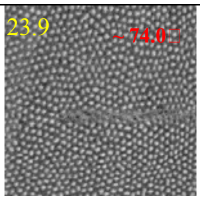 *611a05a*	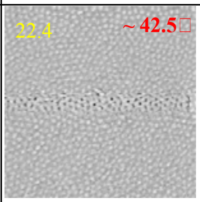 *627a05a*
[PS-*b*-PMMA] 0.75% wt	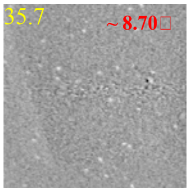 *627a075b*	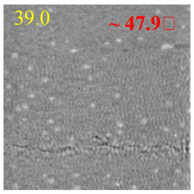 *628a075b*	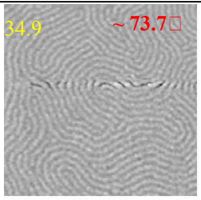 *	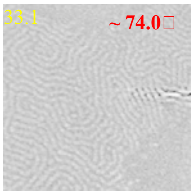 *627a075a*	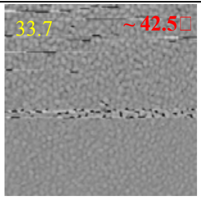 *627a075b*
[PS-*b*-PMMA] 1.0% wt	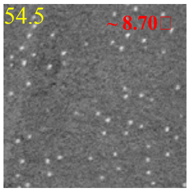 *611a1a*	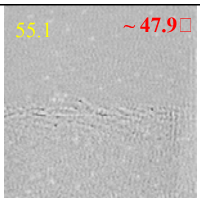 *628a1b*	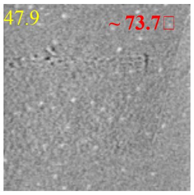 *822a1b*	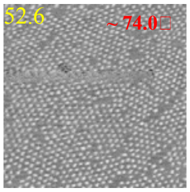 *611a1b*	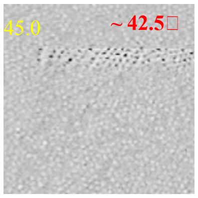 *627a1a*
[PS-*b*-PMMA] 3.0% wt	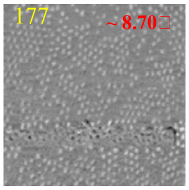 *1120a3*	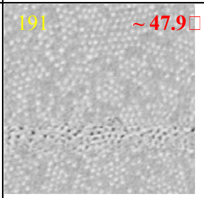 *628b3b*	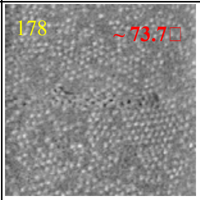 *822a3a*	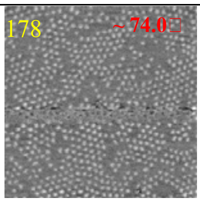 *611a3b*	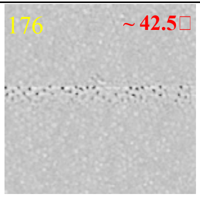 *628a3d*

Files name: a) moi\pspmma\si\o3\, b) moi\pspmma\si\nterm, c) moi\pspmma\si\alkylter\, d) moi\pspmma\si\hf\, e) moi\pspmma\au

Table A-2 On Different Types of Substrates: a) Ozone Exposed, b) Amine Terminated SAM Coated, c) Alkyl Terminated SAM Coated, d) HF Treated, and e) Gold Coated, Set #2.

Film Thickness Before Annealing in nm (yellow), θ^{water} in degree (red).

Substrate	**Si-O$_2$ $^{(a)}$**	**Si-N term $^{(b)}$**	**Si-CH$_3$ term $^{(c)}$**	**Si-HF $^{(d)}$**	**Au-Si $^{(e)}$**
[PS-*b*-PMMA] 0.50% wt	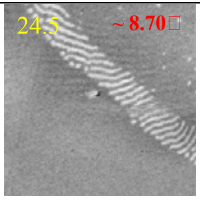 *611b05a*	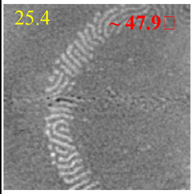 *628b05b*	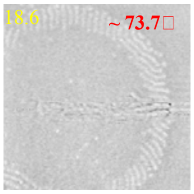 *	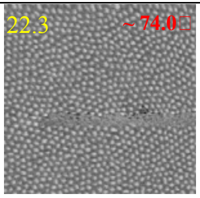 *611a05b*	**
[PS-*b*-PMMA] 0.75% wt	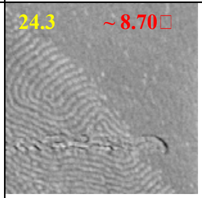 *627b075a*	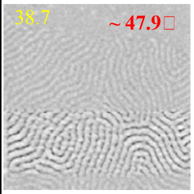 *628b075b*	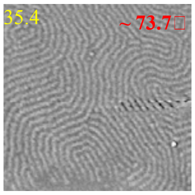 *822a075a*	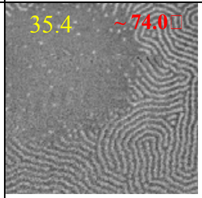 *627b075a*	**
[PS-*b*-PMMA] 1.0% wt	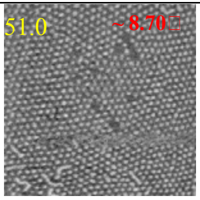 *611b1a*	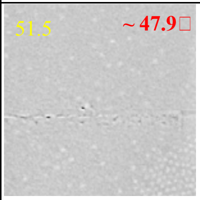 *628b1b*	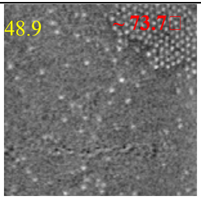 *822a1c*	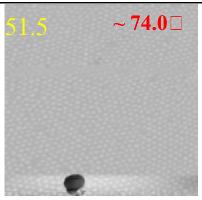 *611b1b*	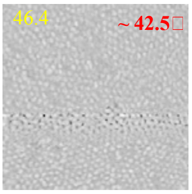 *627b1b*
[PS-*b*-PMMA] 3.0% wt	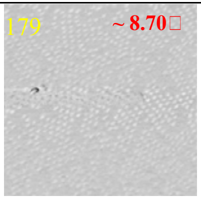 *611b3b*	*	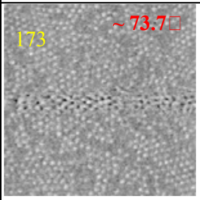 *822a3b*	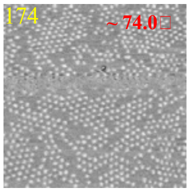 *611b3b*	**

* Unavailable data.

** See Figure 3-1.

Files name: a) moi\pspmma\si\o3\, b) moi\pspmma\si\nterm, c) moi\pspmma\si\alkylter\, d) moi\pspmma\si\hf\, e) moi\pspmma\au